

Quantifying Dyke-Induced Graben and Dyke Structure Using 3D Seismic Reflection Data and the Role of Interpretation Bias

Craig Magee *¹, Victoria Love¹, Karima Fayez¹, Billy J. Andrews ², Sam Rivas-Dorado ³, Christopher A.-L. Jackson ⁴, Claire Orlov ¹, Emma Bramham ¹

¹School of Earth and Environment, University of Leeds, Leeds, UK | ²School of Geography, Earth and Environmental Sciences, University of Plymouth, Plymouth, UK | ³Departamento de Geodinámica, Estratigrafía y Paleontología, Universidad Complutense de Madrid, Madrid, Spain | ⁴Basins Research Group (BRG), Department of Earth Science and Engineering, Imperial College London, London, UK

Abstract During dyke intrusion, tensile stresses concentrated within the overlying rock may lead to the formation of normal faults. These faults typically form graben-bounding pairs that are sub-parallel to, and dip toward, the upper tip of their underlying dyke. Many studies use geometric properties extracted from the surface expression of such dyke-induced faults to estimate the geometry of subsurface dykes. These methods assume dyke-induced faults are planar and nucleate at the surface. However, recent seismic reflection-based investigations of the 3D structure of dyke-induced faults confirm they can be non-planar and have complex growth histories. Here, we use 3D seismic reflection surveys from offshore NW Australia to: (1) examine how the surface expression of dyke-induced faults relates to subsurface dyke geometry and depth; and (2) test whether subjective bias may influence the quantitative analyses of dyke-induced faults using seismic reflection data. We show displacement and dip vary across dyke-induced faults, supporting previous suggestions that faults nucleate between dyke upper tips and the free surface. We also find that prediction of dyke upper tip depths using graben width and area of loss methods are sensitive to fault dip variations and interpretation biases, but often still produce similar results to measured dyke depths. Both measured and predicted dyke depths vary by several hundred metres along-strike, which we relate to the preservation of dyke heads, segmentation, and/or magma density changes. Overall, we show reflection seismology provides a better understanding of the 3D structure of dyke-induced faults and their relationship to the geometry and emplacement dynamics of their causal dykes.

Executive Editor:
R. da Silva Schmitt
Technical Editor:
Mohamed Gouiza

Reviewers:
Juan Alcade
Natasha Stanton

Submitted:
4 November 2022
Accepted:
30 June 2023
Published:
31 July 2023

1 Introduction

Igneous dykes facilitate magma transport and their intrusion generates both extensional and compressional stresses (Figure 1A) (e.g., *Rivalta et al.*, 2015; *Rubin*, 1993). Within the upper crust, dyke intrusion and opening is expected to concentrate tensile stresses above the dyke upper tip and in two elongate, sub-parallel zones at the free surface (Figure 1A) (e.g., *Koehn et al.*, 2019; *Pollard et al.*, 1983; *Rubin*, 1992; *Rubin and Pollard*, 1988). Shear failure within this extensional stress field produces graben-bounding normal faults that strike sub-parallel to the underlying dyke and which extend from the dyke's upper tip to zones of maximum tensile stress at the surface (Figure 1A) (e.g., *Pollard et al.*, 1983; *Trippanera et al.*, 2015a). In many active and ancient volcanic systems, on Earth and other planetary bodies, we can examine the surface expression of such dyke-induced faults and quantify their geometry, displacement, and kinematics (e.g., *Perrin et al.*, 2022; *Pollard et al.*, 1983;

Rivas-Dorado et al., 2021; *Trippanera et al.*, 2015a; *Wilson and Head*, 2002; *Xu et al.*, 2016). We expect these fault properties to relate to the location, size, shape, and intrusion dynamics of the underlying dyke (e.g., *Drymoni et al.*, 2023; *Dumont et al.*, 2017; *Rivas-Dorado et al.*, 2021; *Trippanera et al.*, 2015a). Studying dyke-induced faults thus allows us to infer the structure and dynamics of subsurface dykes, which is crucial to understanding volcanic activity and the role of dyking in crustal extension (e.g., *Dumont et al.*, 2015; *Rivas-Dorado et al.*, 2021; *Tibaldi et al.*, 2022; *Trippanera et al.*, 2015b; *Wilson and Head*, 2002; *Xu et al.*, 2016).

Several previous studies have used the width of dyke-induced graben and fault heaves to estimate the depth to dyke upper tips and dyke thickness, respectively (e.g., *Hjartardóttir et al.*, 2016; *Perrin et al.*, 2022; *Rivas-Dorado et al.*, 2021; *Rubin*, 1992; *Rubin and Pollard*, 1988; *Trippanera et al.*, 2015b). These predictions assume that dyke-induced faults are planar and project down-dip to intersect at the dyke upper tip (Figure 1A), and that their cumulative heaves

*✉ c.magee@leeds.ac.uk

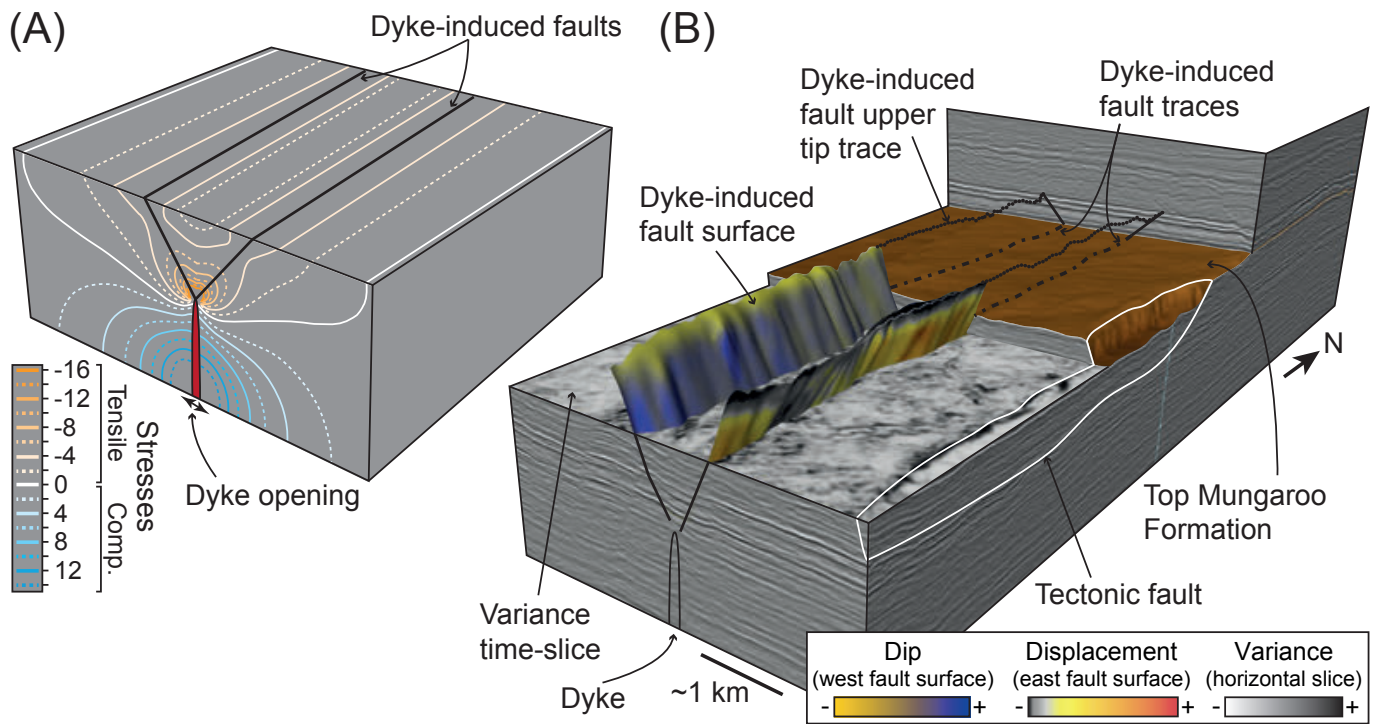


Figure 1 – (A) Schematic 3D block diagram showing the modelled stress distribution around an opening dyke, and the location of expected dyke-induced faults (based on *Rubin, 1992*). (B) 3D seismic reflection data from the Chandon 3D seismic survey, offshore NW Australia, detailing the seismic expression of dykes and dyke-induced faults (based on *Magee and Jackson, 2020*). Fault dip and displacement variations are shown on the opposing faults

are broadly equivalent to dyke thickness (e.g., *Magee and Jackson, 2021*). Physical, numerical, and analytical models support these assumptions (e.g., *Hardy, 2016; Koehn et al., 2019; Mastin and Pollard, 1988; Pollard et al., 1983; Tripanera et al., 2015b*), but it is difficult to test their validity because: (1) we lack field exposures that reveal the 3D structure of dyke and dyke-induced fault systems; and (2) models of ground movement related to active dyke-induced faulting are typically non-unique (e.g., *Wright et al., 2006*).

Reflection seismology allows us to image entire dyke and dyke-induced fault systems in 3D at a decametre-scale (Figure 1B) (*Bosworth et al., 2015; Magee and Jackson, 2021, 2020*). For example, using seismic reflection data from offshore NW Australia, *Magee and Jackson (2021)* show that fault displacement, heave, and dip varied laterally and vertically across two buried dyke-induced faults (Figure 1B): dyke-induced faults are thus not always planar, as is commonly assumed, and their surficial heave may not fully reflect the extension the faults accommodate. These findings question the accuracy of dyke locations, sizes, and shapes estimated from the surface expression of dyke-induced faults (*Magee and Jackson, 2021*). However, extracting quantitative data (e.g., dyke-induced fault properties) from seismic reflection data is subject to several objective and subjective sources of uncertainty (e.g., *Alcalde et al., 2017a; Bond et al., 2007; Dimmen et al., 2023; Faleide et al., 2021; Wilson et al., 2019*). We thus need to establish how sources of uncertainty may affect interpretation of dyke-induced fault data extracted from seismic reflection volumes, if we are to have confidence in mod-

els derived from these data.

Here, we use two 3D seismic reflection datasets from offshore NW Australia to extend the study of *Magee and Jackson (2021)*. We specifically test: (1) if other dyke-induced fault pairs in the region show similar variations in displacement and dip across their surface (e.g., Figure 1B) (*Magee and Jackson, 2021*); (2) the reliability of different methods for estimating dyke upper tip depths, which we refer to as top-dyke depths, from dyke-induced graben geometry (e.g., *Pollard et al., 1983; Rivas-Dorado et al., 2021; Tripanera et al., 2015b*); and (3) how sources of uncertainty affect variations in measured or calculated fault, graben, and dyke properties (e.g., *Bond et al., 2007; Faleide et al., 2021*). To achieve our aims, we compile and calculate fault property data from foot-wall and hanging wall cut-offs mapped by four individuals from the same faults. We present data for dyke-induced fault pairs above three dykes and show displacement and dip is variable across them all, consistent with the findings of *Magee and Jackson (2021)*. Although interpretation bias can introduce measurement errors, consistency between datasets produced by different individuals suggests we can, at least to a first order, relate the surface expression of dyke-induced faults to dyke geometry (cf. *Magee and Jackson, 2021*). However, it seems that building confidence in estimating dyke parameters from related ground deformation requires knowledge of how fault properties, particularly dip, change with depth. Unfortunately, this subsurface information is rarely available for active volcanic settings or other planetary bodies, but we suggest empirical data and

relationships derived from reflection seismic data could help reduce uncertainty.

2 Geological Setting

The Northern Carnarvon Basin, located offshore NW Australia, developed during several phases of rifting between Australia and Greater India in the Late Carboniferous-to-Early Cretaceous (Figure 2) (e.g., *Direen et al.*, 2008; *Stagg et al.*, 2004; *Tindale et al.*, 1988). Within this basin, the Exmouth Plateau is located towards the south-west and marks a region of <10 km thick continental crust overlain by a <18 km thick sedimentary sequence (Figure 2C) (e.g., *Exon et al.*, 1992; *Karner and Driscoll*, 1999; *Pryer et al.*, 2002). Rifting of the Exmouth Plateau began in the Late Triassic-to-Jurassic, forming an array of ~N-S striking, large (often >1 km throw) normal faults within pre-rift, fluvio-deltaic sedimentary rocks of the Mungaroo Formation (Figure 2B and C) (e.g., *Bilal and McClay*, 2022; *Bilal et al.*, 2018; *Stagg et al.*, 2004). The Exmouth Plateau was sediment-starved during this phase of rifting, so contains a relatively condensed (~100 m thick), late Triassic-to-Early Jurassic marine succession (e.g., Figure 2B and C) (e.g., *Exon et al.*, 1992; *Karner and Driscoll*, 1999). This latest Triassic-to-Early Jurassic strata is separated from the Late Jurassic, marine Dingo Claystone by the end Callovian regional unconformity (Figure 2B) (e.g., *Bilal et al.*, 2018; *Tindale et al.*, 1988; *Yang and Elders*, 2016). Tectonic faulting reduced or ceased in the Late Jurassic across the North Carnarvon Basin, but renewed after formation of the Base Cretaceous unconformity (latest Tithonian; ~148 Ma) and during deposition of the Tithonian–Valanginian (~148–138 Ma), marine Barrow Group (Figure 2B) (e.g., *Gartrell et al.*, 2016; *Pau-mard et al.*, 2018; *Reeve et al.*, 2016). This renewed faulting produced N-S to NE-SW-striking, low-throw (<0.1 km) normal faults (e.g., *Black et al.*, 2017). Continental break-up eventually occurred along the western and southern margins of the Exmouth Plateau in the Early Cretaceous (Valanginian–Hauterivian; ~135–130 Ma), followed by thermal subsidence and passive margin development (Figure 2B and C) (e.g., *Direen et al.*, 2008; *Reeve et al.*, 2021; *Robb et al.*, 2005).

2.1 The Exmouth Dyke Swarm and Dyke-Induced Faults

Seismic reflection data reveal a swarm of sub-vertical, low-amplitude zones that disrupt stratigraphic reflections within (and below) the Mungaroo Formation across the Exmouth Plateau (e.g., Figures 1B and 3) (*Magee and Jackson*, 2021). Borehole data confirm these vertical zones of disruption correspond to dykes, each likely 10's of metres thick, belonging to the Exmouth Dyke Swarm (*Magee and Jackson*, 2021). These dykes are 10's–100's km long and appear to radiate outwards from focal area within the Cuvier Margin, from which they likely propagated laterally northwards (e.g., Figure 2A) (*Magee and Jackson*, 2021). A series of graben occur directly above and along the

dykes, with the oppositely dipping faults intersecting at the dyke upper tips (e.g., Figures 1B and 3); these have been interpreted as dyke-induced faults (*Magee and Jackson*, 2020, 2021). The dyke-induced faults offset siliciclastic Triassic-to-Jurassic strata, and terminate upwards at the Base Cretaceous unconformity, which is inferred to mark the free surface at the time of faulting and dyking (e.g., Figure 3A and B) (*Magee and Jackson* 2020a; *Magee and Jackson* 2020b). Within the dyke-induced graben are numerous pit craters, which extend from dyke upper tips or dyke-induced fault planes up into the Upper Jurassic Dingo Claystone (e.g., Figure 3B) (*Magee and Jackson*, 2020, 2021). Seismic reflection data reveal a swarm of sub-vertical, low-amplitude zones that disrupt stratigraphic reflections within (and below) the Mungaroo Formation across the Exmouth Plateau (e.g., Figures 1B and 3) (*Magee and Jackson*, 2020). Borehole data confirm these vertical zones of disruption correspond to dykes, each likely 10's of metres thick, belonging to the Exmouth Dyke Swarm (*Magee and Jackson*, 2020). These dykes are 10's–100's km long and appear to radiate outwards from focal area within the Cuvier Margin, from which they likely propagated laterally northwards (e.g., Figure 2A) (*Magee and Jackson*, 2020). A series of graben occur directly above and along the dykes, with the oppositely dipping faults intersecting at the dyke upper tips (e.g., Figures 1B and 3); these have been interpreted as dyke-induced faults (*Magee and Jackson*, 2020, 2021). The dyke-induced faults offset siliciclastic Triassic-to-Jurassic strata, and terminate upwards at the Base Cretaceous unconformity, which is inferred to mark the free surface that was concurrent with fault and dyke activity (e.g., Figure 3A and B) (*Magee and Jackson*, 2020, 2021). Within the dyke-induced graben are numerous pit craters, which extend from dyke upper tips or dyke-induced fault planes up into the Upper Jurassic Dingo Claystone (e.g., Figure 3B) (*Magee and Jackson*, 2020, 2021).

3 Data and Methods

3.1 Data

We use the Chandon and Glencoe 3D seismic reflection surveys to analyse dyke-induced faults above three dykes (dykes B, D, and E; Figure 3). Both seismic surveys are time-migrated, processed to zero-phase, and have bin spacings of 25 m; Chandon has a record length of 6 seconds two-way time (s TWT), whereas Glencoe extends down to 8 s TWT. The Chandon 3D survey has a SEG reverse polarity, whereby a downward increase in acoustic impedance corresponds to a trough (black) reflection and a downward decrease in acoustic impedance is marked by a peak (white) reflection (Figure 3A). Conversely, the Glencoe 3D survey has an SEG normal polarity (Figure 3B).

To constrain the age and lithology of mapped reflections, we tied four and five different boreholes to the Chandon and Glencoe 3D surveys, respectively (Figure 3C). Checkshot data from these bore-

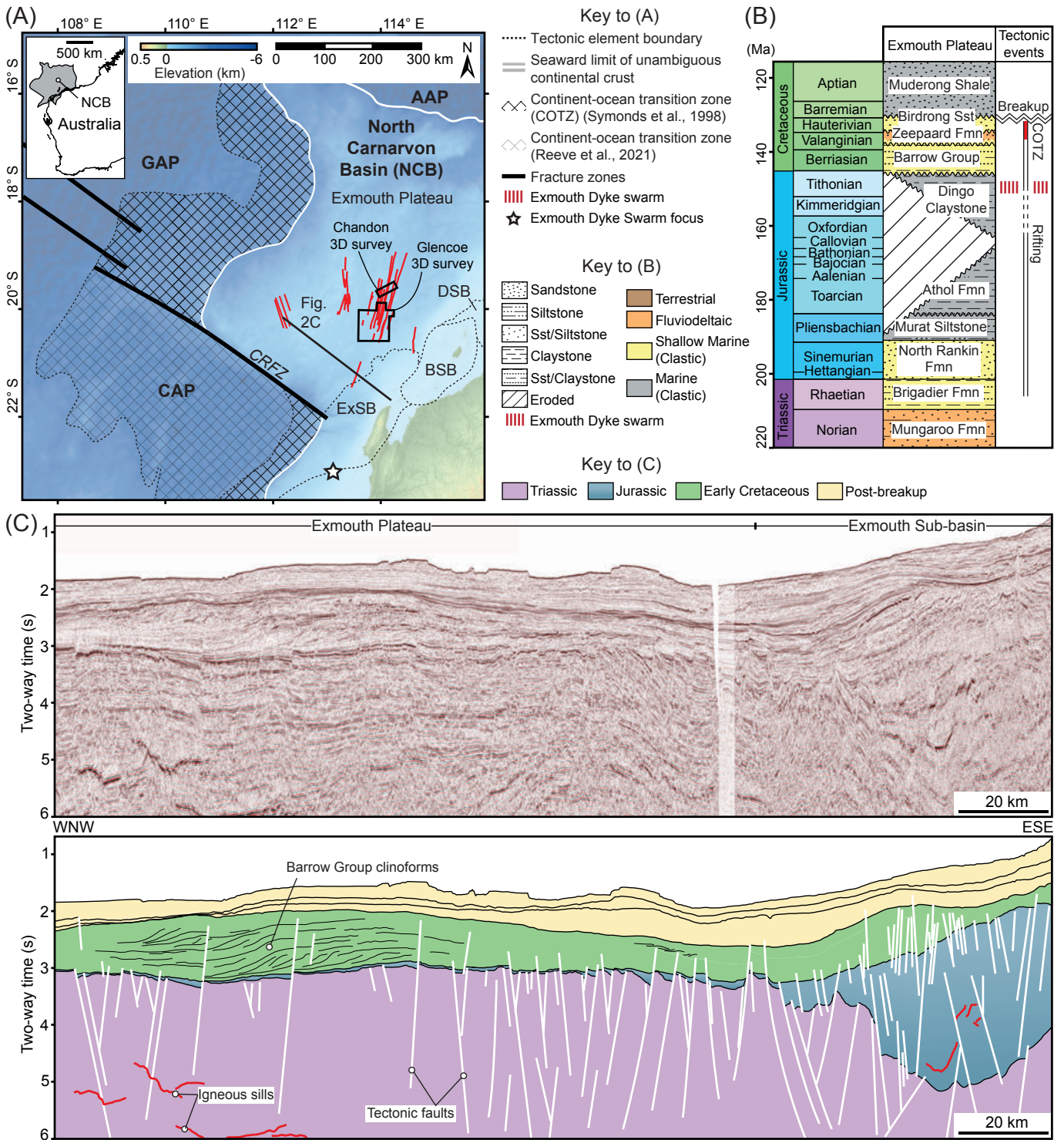


Figure 2 – (A) Map of offshore NW Australia highlighting principal tectonic elements: ExSB = Exmouth Sub-basin, BSB = Barrow Sub-basin, DSB = Dampier Sub-basin, CAP = Cuvier Abyssal Plain, GAP = Gascoyne Abyssal Plain, AAP = Argo Abyssal Plain, CRFZ = Cape Range Fracture Zone. Elevation data are based on the 2009 Australian Bathymetry and Topography grid (Geoscience Australia). The Exmouth Dyke Swarm is also shown (Magee and Jackson, 2021). (B) Tectono-stratigraphic column for the Exmouth Plateau (based on Hocking et al., 1987; Magee and Jackson, 2021; Longley et al., 2002; Tindale et al., 1988). (C) Uninterpreted and interpreted 2D seismic line across the Exmouth Plateau and Exmouth Sub-basin showing the upper part of the sedimentary sequence (modified from Norcliffe et al., 2021).

holes allowed us to establish time-depth relationships for the two seismic surveys (Figure SI-1 and Table SI-1, in Supporting Information), which we use to depth-convert measurements from TWT to metres. With these time-depth relationships and dominant frequencies of ~40–30 Hz within the interval of inter-

est, we estimate the limits of separability and visibility for both datasets to be ~20±4 m and 3±1 m, respectively. The limit of separability defines the smallest vertical distance between two boundaries for them to be expressed in the data as discrete reflections (e.g., Brown, 2011). Acoustic energy reflected from

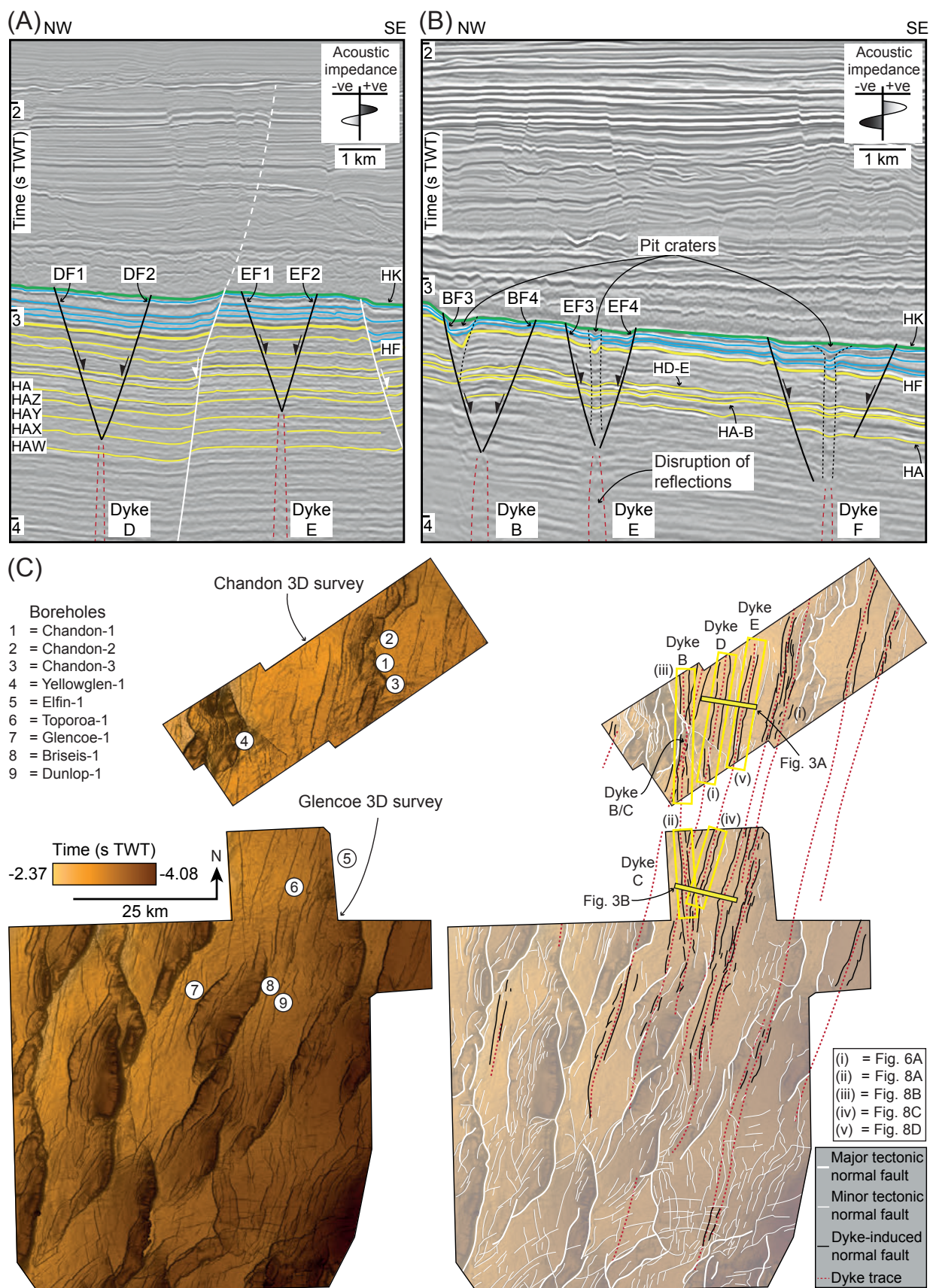


Figure 3 – (A and B) Interpreted seismic sections showing dykes, dyke-induced faults, and stratigraphic horizons (HK–HAW) mapped in the Chandon and Glencoe 3D surveys. Yellow horizons are Triassic, blue horizons are Jurassic, and the green horizon marks the Base Cretaceous Unconformity (HK). Some tectonic faults and pit craters are also highlighted (Magee and Jackson, 2021). Line locations shown in (C) and insets show how a downwards positive (+ve) or negative (-ve) change in acoustic impedance affects reflection colour. Uninterpreted sections shown in (Figure S1-2, in Supporting Information). **(C)** Uninterpreted and interpreted time-structure map of the Top Mungaroo Formation (horizon HF) in the Chandon and Glencoe 3D surveys, with tectonic and dyke-induced faults marked. Boreholes used in the study as well as underlying dyke traces are also shown (Magee and Jackson, 2021).

boundaries separated by vertical distances less than the limit of separability, but greater than the limit of visibility, merges on their return to the surface and cannot be deconvolved; this produces a tuned reflection package, as opposed to two distinct reflections (e.g., *Brown, 2011*). For any boundaries separated by a vertical distance (throw) less than the limit of visibility, their reflection signal is obscured by seismic noise (*Brown, 2011*). The horizontal resolution of both datasets is ~25 m, equivalent to the bin spacing.

3.2 Seismic Interpretation

To test the findings of *Magee and Jackson (2021)*, which focussed on the dyke-induced faults above Dyke E in the Chandon 3D survey, we extend their mapping of 11 seismic horizons (HA–HK; Figure 3A) to areas above dykes B and D, which are imaged in the Chandon 3D survey. Of these horizons, HK corresponds to the Base Cretaceous unconformity and HF defines the Top Mungaroo Formation (Figure 3A). The upper tip of some dykes we analyse are deeper than that of Dyke E, and their overlying dyke-induced faults extend to greater depths too; we thus also map several horizons below HA (i.e. HAZ–HAW; Figure 3A). Where possible within the Glencoe 3D survey, we map the same HK–HA horizons above dykes B, D, and E (Figure 3B). However, due to variations in data quality and reflection continuity within the Glencoe volume, we cannot map horizon HE and instead interpret a deeper reflection we name HD-E (Figure 3B). In the Glencoe volume we also map an extra horizon, HA-B, between HA and HB (Figure 3B).

Using transects oriented perpendicular to fault strike and dyke trend, we measure the hanging wall and footwall cut-off pairs for each horizon, where they intersect the studied dyke-induced faults, and the upper tips of underlying dykes (e.g., Figure 4A). Four of the authors independently mapped fault cut-offs and dyke tips along the same selected graben (Craig Magee = CM; Victoria Love = VL; Karima Fayez = KF; Billy Andrews = BA), allowing us to assess the impact of interpretation bias on our findings. Transect spacing is 100 m for BA and 125 m for CM, VL, and KF; these values were selected to provide a high-resolution dataset in a suitable timeframe, with the 100 m and 125 m spacings used to check whether line selection influenced results.

3.3 Measurements and Calculations

From the coordinates of each interpreted fault cut-off pair, including those mapped by *Magee and Jackson (2021)*, we calculate fault throw (t) and heave (h) (Figure 4A). These throw and heave calculations allow us to estimate fault dip (α) and displacement (d), assuming the slip vector is dip-parallel (Figure 4A) (*Magee and Jackson, 2021*). There is no evidence within the seismic reflection data to support or challenge the assumption that the dyke-induced fault slip vectors were dip-parallel, but this is broadly consistent with observations of tensile opening and slip vectors of

active dyke-induced faults observed elsewhere (e.g., *Hofmann, 2013; Tibaldi et al., 2022*). For fault cut-offs mapped on faults along the same horizon and transect, we combine fault property measurements to derive cumulative throw, heave, and displacement values, as well as the average fault dip (α_{av}). Along each transect, we also use fault cut-off coordinates to calculate (Figure 4A): (1) the horizontal graben width (G_W) and half-width (G_{WH}) between footwall cut-offs; (2) the line length distance (G_L) between footwall cut-offs, which unlike G_W or G_{WH} accounts for differences in cut-off elevation; (3) the horizontal graben width (g_w) between hanging wall cut-offs; (4) the line length distance (g_l) between the hanging wall cut-offs; and (5) the diagonal line length (G_{DIA}) between one hanging wall cut-off and the opposing footwall cut-off (see also *Rivas-Dorado et al., 2021*). These graben width and line length measurements are required to calculate the graben area on each transect (*Rivas-Dorado et al., 2021*).

We apply two methods to predict the current (D_D^n ; i.e. the predicted depth of the dyke below the current seabed) and syn-emplacement (D_D^0 ; i.e. the predicted depth of the dyke below horizon HK, the seabed concurrent to dyke intrusion) top-dyke depths from calculated graben width properties (Figure 4). We first use trigonometry to estimate top-dyke depths from graben half-widths (G_{HW}) and fault dips (α) measured at any stratigraphic level, such as the syn-emplacement free surface (Figure 4B) (e.g., *Pollard et al., 1983; Trippanera et al., 2015b*). This trigonometric method assumes faults are planar and project straight down-dip (Figure 4B) (*Magee and Jackson, 2021*). Most studies assume α is constant for both faults and, based on measurements and/or regional information, is ~70–60° (e.g., *Rubin and Pollard, 1988; Trippanera et al., 2015a*). We present results where we consider that both faults have dips equivalent to either: (1) the average of the two fault dips (α_{av}); (2) 60°, as this is thought typical of normal faults within an Andersonian framework (*Anderson, 1951*); and (3) 45°, which is similar to the dip of Late Jurassic-to-Early Cretaceous tectonic normal faults in the region (e.g., *Magee et al., 2016*). We henceforth refer to these three method variants as $\text{trig}_{\alpha_{av}}$, trig_{60} , and trig_{45} , respectively. We also use an area of loss method, which relates the cross-sectional area of a graben on a given transect to the top-dyke depth (*Rivas-Dorado et al., 2021*). The area of loss method specifically calculates the area between the four fault cut-offs on each transect, which form the vertices of an irregular quadrilateral shape, using the defined line length measurements G_L , g_l , and G_{DIA} (Figure 4A, C) (*Rivas-Dorado et al., 2021*). From the area of this irregular quadrilateral shape, a rectangle of the same area is created (*Rivas-Dorado et al., 2021*). By setting the width of this derived rectangle to equal the cumulative fault heave, which is assumed equivalent to dyke thickness (DT), the resulting length of the rectangle is taken as the vertical distance between the syn-emplacement surface and dyke upper tip (Figure 4C); i.e. the graben

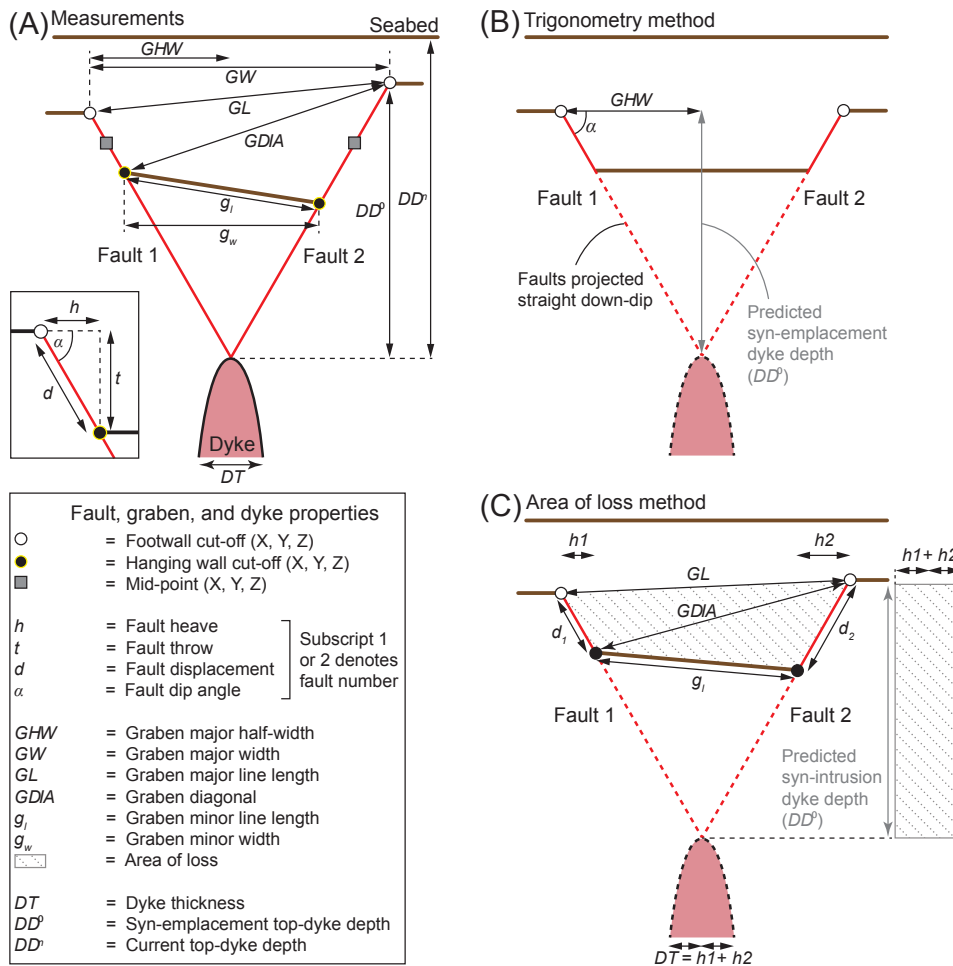


Figure 4 – (A) Schematic diagram depicting the different dyke-induced fault and graben properties calculated from the X, Y, and Z co-ordinates of mapped fault-cut-offs. **(B)** Sketch showing how fault dips and graben half-widths can be used to project faults down-dip and estimate dyke upper tip depths. **(C)** Sketch showing the graben area of loss and cumulative fault heave ($h_1 + h_2$) can be used to define a rectangle, the length of which can be considered equivalent to the dyke upper tip depth (modified from *Rivas-Dorado et al., 2021*).

area of loss is assumed to equal the area gained by dyke-driven extension (*Rivas-Dorado et al., 2021*).

3.4 Limitations and Errors

Although seismic reflection data provide unique insight into the 3D structure of dykes and dyke-induced faults, interpreting and quantitatively assessing these features, which often have displacements of <20 m, is affected by several objective and subjective uncertainties involved in seismic interpretation (e.g., *Dimmen et al., 2023; Magee and Jackson, 2021; Wilson et al., 2019*). Objective uncertainty, which can often be quantified, includes limitations related to resolution and quality of seismic imaging, as well as seismic velocities used for depth conversion (*Faleide et al., 2021*). For example, the seismic velocities we use are taken from borehole data, meaning they do not capture possible variations in seismic velocity across the study area, away from the borehole locations (*Magee and Jackson, 2021*). However, because the time-depth relationships of the boreholes for each 3D survey we use are similar (Figure SI-1, in Supporting Information), we adopt the conservative view that calculated seismic velocities could vary by up to $\pm 10\%$ (*Magee*

and Jackson, 2020, 2021).

It is also important to consider that the dykes and dyke-induced faults in the Exmouth Plateau formed during the Late Jurassic, and have since been buried by several kilometres of sedimentary strata (*Magee and Jackson, 2020*). Most sedimentary rocks compact as they are buried, reducing stratal thicknesses and rotating any pre-existing, inclined fractures to shallower angles (*Allen and Allen, 2013*). Burial-related compaction can thus reduce fault throw, potentially by up to 15% in sand-dominated or mixed sand-shale lithologies (*Taylor et al., 2008*), meaning our calculated fault dips, displacements, and predicted top-dyke depths are minimum estimates. However, we note that all dykes and dyke-induced faults in the study area occur at similar depths (~3–4 km) under a similar overburden thickness, so we suggest compaction, and compaction-related modification of the primary geometries, can be considered to have been constant across the study area (*Magee and Jackson, 2020, 2021*). Although our measurements and calculations may not therefore reflect the absolute syn-emplacement 3D structure of the dyke and dyke-induced faults, their relative values will be compara-

ble, i.e. the current patterns of displacement, dip, or predicted dyke upper tip depth distribution will be the same as when dyking occurred in the Late Jurassic.

Subjective uncertainties and biases relate to those introduced by the person undertaking the interpretation and are generally more difficult to quantify (e.g., *Alcalde et al., 2017a; Bond et al., 2007; Faleide et al., 2021; Wilson et al., 2019*). For example, mapping footwall and hanging wall cut-offs of low offset faults, or faults with a high proportion of continuous deformation, is particularly prone to interpretation bias (*Schaaf and Bond, 2019*). Where fault displacement is substantially greater than the limit of separability and horizontal resolution, reflections are often clearly offset and discrete footwall and hanging wall cut-offs can be identified (Figure 5A and B) (*Dimmen et al., 2023*). In these cases, any fault-related continuous deformation (i.e. local rotation of bedding and thus reflections adjacent to faults; *Delogkos et al., 2017*) can be accounted for by projecting the regional dip of horizons onto the fault to define cut-off positions (Figure 5A and C) (e.g., *Mansfield and Cartwright, 1996*). In contrast, where fault displacement is close to or below the limit of separability and horizontal resolution, reflections are continuous but appear locally distorted (Figure 5A and D) (e.g., *Dimmen et al., 2023; Faleide et al., 2021*). Here, it is the interpreter's decision, which can be biased by experience (e.g., *Bond et al., 2007*), as to where to place the footwall and hanging wall cut-offs (Figure 5D). For example, an interpreted portion of the fault will have a shallower dip and larger displacement (and heave) if cut-offs are mapped at the inflection points of a distorted reflection, as opposed to projecting the cut-offs to a midpoint (Figure 5D). Any projection of cut-offs also influences measured graben width properties. Given limitations of data resolution and imaging quality, there is no unique, or 'correct', interpretation of fault cut-off location (*Alcalde et al., 2017a; Dimmen et al., 2023; Faleide et al., 2021, e.g.,*).

Previous studies have suggested interpretation bias in quantifying dyke-induced fault properties can be conservatively accounted for by applying $\pm 5\%$ measurement errors (*Magee and Jackson, 2021*). To preliminarily explore the effect of interpretation bias, and test these prior assumptions, we present data based on independent mapping of fault cut-offs by four authors (CM = Craig Magee; VL = Victoria Love; KF = Karima Favez; BA = Billy Andrews). Each author mapped fault cut-offs along the Top Mungaroo Formation for one or several dyke-induced fault pairs, using different transects and transect spacings relative to others. We also conducted a repeat experiment whereby CM mapped dyke-induced fault cut-offs above Dyke D along the Top Mungaroo Formation on the same transects on two occasions (CM1 and CM2), separated by ~ 1 year. To compare the results from these datasets, we use F-tests to statistically determine the probability that calculated fault properties or predicted dyke upper tip depths are not significantly different. If the calculated F value for the

two or three datasets being compared is less than a critical amount (F_{crit}), the null hypothesis that the datasets may be considered equal is accepted.

4 Results

4.1 Structural Framework

Dykes D and E are sub-parallel and strike $\sim 012^\circ$ (Figure 3C). Dyke B and its dyke-induced faults trend $\sim 002^\circ$, intersecting other dykes (i.e. C, D, and E) and associated faults, respectively (Figure 3C). Where these dykes and faults intersect, they can be difficult to identify and assign (Figure 3C). Dyke B and its dyke-induced faults also cross-cut or are cross-cut by a major W-dipping, $\sim N-S$ striking, tectonic normal fault, and several smaller associated tectonic faults within the Chandon 3D survey (Figure 3C). Within the Chandon 3D survey, dyke-induced faults above Dyke D are also cross-cut, and possibly offset by, a minor S-dipping, $\sim NW-SE$ striking, tectonic normal fault (Figures 3C and 6A). Elsewhere in the study area, there is little connectivity between the studied dyke-induced faults and tectonic faults (Figure 3C).

4.2 Dyke D and its Overlying Dyke-Induced Faults

To illustrate our research methodology, we first present quantitative data from the dyke-induced faults above Dyke D in the Chandon 3D survey, which we separate into DF1-DF2 and DF3-DF4 pairs, analysed by CM and BA (Figure 6A); two cut-off sets are mapped by CM (i.e. CM1 and CM2; Figure 6). Above Dyke D along the Top Mungaroo Formation, graben widths are $\sim 1.20-2.05$ km, average fault dips are $\sim 20-85^\circ$, and cumulative displacements are $\sim 5-97$ m (Figure 6; Table SI-2, In Supporting Information). Dyke-induced fault lengths mapped by CM and BA differ, with CM interpreting DF1-DF2 ~ 3 km further northwards than BA (Figure 6A). Where fault cut-offs interpreted by CM and BA spatially overlap, graben widths are similar, displaying systematic increases and decreases along-strike at the kilometre-scale (Figure 6B). The average fault dips and cumulative displacement calculated by CM1, CM2, and BA are more variable (Figure 6C and D; Table SI-2, In Supporting Information). Differences between the CM1 and CM2 datasets, which use the same transects, are due to small offsets of ~ 100 m in cut-off positions (average is ~ 18 m; Table SI-3, In Supporting Information) but statistical F-tests reveal their variance is insignificant (i.e. $F < F_{crit}$; Table 1). Conversely, F-tests demonstrate that variances between the CM1, CM2, and BA measurements of graben width, average fault dip, and cumulative displacement are significant (i.e. $F > F_{crit}$; Table 1).

Measured top-dyke depths for Dyke D in the Chandon 3D survey range from $\sim 3.5-3.8$ km beneath current sea-level (Table SI-2, In Supporting Information), which broadly correspond to emplacement depths of $\sim 0.9-1.1$ km beneath the syn-intrusion surface,

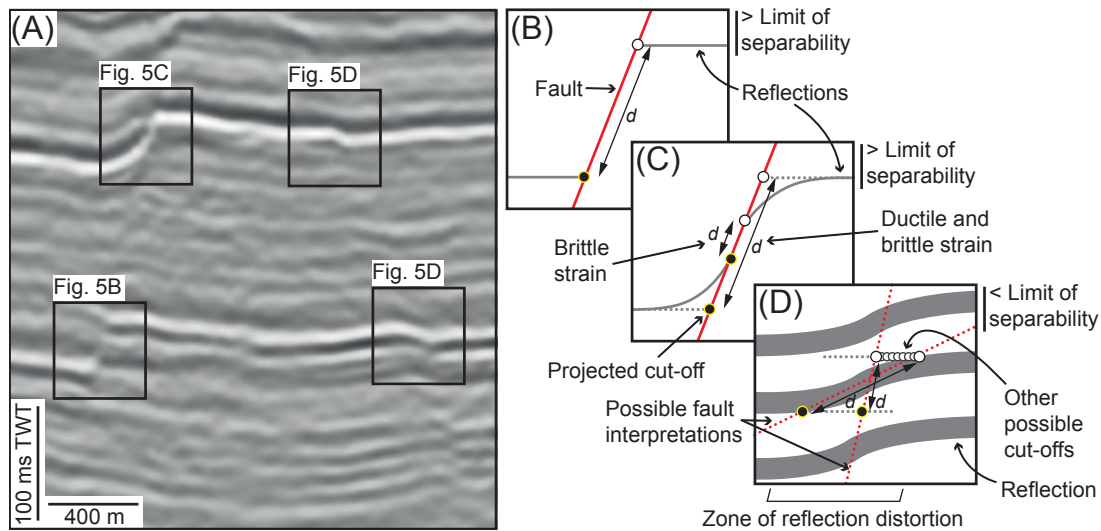


Figure 5 – (A) Uninterpreted seismic section from the Chandon 3D survey showing different reflection configurations across two faults. (B-D) Schematic diagrams describing how and where fault footwall and hanging wall cut-offs may be interpreted for the different reflection-fault interactions in (A) (e.g., Dimmen et al., 2023)

Table 1 – Statistical F-tests comparing CM1, CM2, and BA data

Property	Interpreter	Mean (m)	Variance	CM1 and CM2 comparison		CM1, CM2, and BA comparison	
				F	F _{crit}	F	F _{crit}
Horizontal graben width [G _w]	CM1	1658	011843	1.01	1.35	14.58	3.02
	CM2	1679	011904				
	BA	1602	010577				
Average fault dip [α_{av}]	CM1	0040	000038	1.36	1.37	35.78	3.02
	CM2	0037	000052				
	BA	0046	000102				
Cumulative displacement	CM1	0036	000167	1.35	1.35	31.87	3.02
	CM2	0034	000225				
	BA	0050	000365				
Trig α_{av} estimated top-dyke depth	CM1	3556	029921	1.02	1.37	26.45	3.02
	CM2	3501	030500				
	BA	3778	205831				
Trig60 estimated current top-dyke depth	CM1	4282	008973	1.04	1.35	08.98	3.02
	CM2	4300	009292				
	BA	4246	008696				
Trig45 estimated current top-dyke depth	CM1	3675	003510	1.04	1.35	05.23	3.02
	CM2	3686	003649				
	BA	3660	003217				
Area of loss estimated current top-dyke-depth	CM1	3547	040773	1.50	1.35	21.90	3.02
	CM2	3488	027126				
	BA	3735	197886				

Horizon HK (Figure 7A). Along the graben, over lateral distances of ~125–250 m, there are some abrupt changes of up to ~200 m in measured top-dyke depth superimposed onto subtle (<100 m) increases and decreases over the kilometre-scale (Figure 7A). Predictions of current top-dyke depths derived using the trig α_{av} , trig45, and area of loss methods are often within error of measured top-dyke depths for both CM and BA (Figure 7; Table SI-2, In Supporting Information). However, top-dyke depths predicted using the trig60 method appear to overestimate dyke depths (Figure 7A). Statistical F-tests reveal the variance of trig α_{av} , trig60, and trig45 calculations by CM1 and CM2 is insignificant (Table 1). Only for top-dyke depths predicted using the area of loss method is the

variance significant (Table 1). F-tests demonstrate the difference between the CM and BA top-dyke depth estimates is significant, regardless of the prediction method used (Table 1). Overall, for Dyke D it appears that the methods of trig α_{av} , trig45, and area of loss provide consistent results, but the derived depth is sensitive to the interpreter collecting the data.

We also measure graben width and predict top-dyke depths using fault cut-offs for DF1-DF2 and DF3-DF4 mapped at various stratigraphic horizons (e.g., Figure 8). As part of the CM1 analysis, we show graben width is variable along DF1-DF2 and DF3-DF4 at all stratigraphic levels and decreases with depth (Figure 8A) (data provided in Magee and Love, 2021).

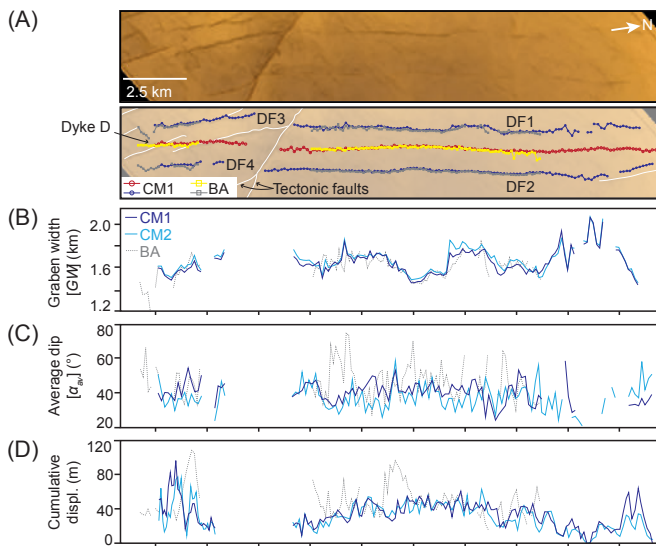


Figure 6 – (A) Uninterpreted and interpreted time-structure map of the Top Mungaroo Formation (horizon HF) above Dyke D in the Chandon 3D survey (see Figure 3C for key and location). Footwall cut-off and dyke upper tip depth locations mapped by CM1 and BA are shown. (B–D) Plots compare graben width, average fault dip, and cumulative displacement (displ.) calculated from CM1, CM2, and BA cut-off mapping.

Top-dyke depths, relative to current sea-level, predicted from these graben width measurements at different stratigraphic levels do vary, but together define a mean profile with relatively low standard deviations of ± 300 m (e.g., Figure 8B and C). Comparing the mean top-dyke depth estimates with those measured from the seismic reflection data reveals that: (1) predictions derived from the $\text{trig}\alpha_{av}$, $\text{trig}45$, and area of loss methods are broadly comparable to measured top-dyke depths, although on average they underestimate top-dyke depths by ± 170 m; and (2) the $\text{trig}60$ predictions are now within the error of measured top-dyke depths, but overestimate measured values by ~ 420 m (Figure 7D).

4.3 Graben Widths along the Top Mungaroo Formation and Predicted Top-Dyke Depths

To further test how interpreter bias may influence quantitative dyke-induced fault analyses, we examine how graben width measurements and predicted top-dyke depths for dykes B and E vary between three authors (i.e. CM, VL, and KF; Figure 9) (all data available in Magee et al., 2022; Magee and Love, 2021). Across the Top Mungaroo Formation (Horizon HF), we observe both gradual changes along-strike in graben width and abrupt changes (e.g., Figure 9). Most measurements of graben width at the Top Mungaroo Formation obtained by different authors are similar (i.e. < 100 m difference) but can vary by up to ~ 400 m (Figure 9A and B). Comparing measured top-dyke depths and those predicted using the graben widths measured along the Top Mungaroo Formation above of dykes B and E reveals that (Figure 9): (1) predicted

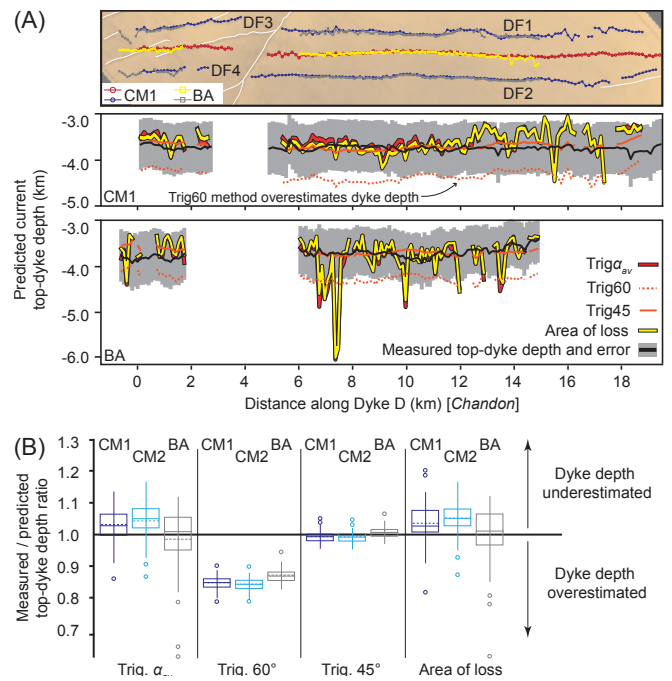


Figure 7 – (A) Plots comparing measured top-dyke depths with those predicted by CM1 and BA using different methods ($\text{trig}\alpha_{av}$, $\text{trig}60$, $\text{trig}45$, and area of loss). Error bars are not shown because we compare calculations subject to the same uncertainties and to improve clarity; we make an exception for the measured top-dyke depths, for which we include a $\pm 15\%$ error envelope, to enable a broader comparison to predicted top-dyke depths. (B) Box-and-whisker plots comparing measured and predicted top-dyke depth ratios calculated by different methods and using fault cut-off datasets mapped by different interpreters (CM1, CM2, and BA). The boxes describe the interquartile range and median of each dataset, with the whiskers marking lower and upper extremes of the data. We also show the mean (dashed line) and outliers in these data.

top-dyke depths derived from the $\text{trig}\alpha_{av}$, $\text{trig}45$, and area of loss methods are broadly comparable to measured top-dyke depths; (2) top-dyke depth predictions calculated using the $\text{trig}60$ method overestimates measured top-dyke depths; (3) even though the four authors mapped fault cut-offs on different transects, there is generally good agreement in their predicted top-dyke depths, except for EF3-EF4; (4) top-dyke depths appear to increase and decrease by ~ 100 m over several kilometres; and (5) abrupt and isolated changes in predicted top-dyke depths along individual graben occur when calculated using the $\text{trig}\alpha_{av}$ and area of loss methods, but are absent when fault dip is assumed to be 60° or 45° . Statistical F-tests reveal that the variance between graben width measurements acquired by different authors above the same fault are not significant (i.e. $F < F_{crit}$; Table 2). We also show that variance between top-dyke depth predictions for Dyke E in the Chandon 3D survey is insignificant ($F < F_{crit}$), but for the Glencoe 3D survey most predictions are significantly different from each other ($F > F_{crit}$), except where we use the area of loss method.

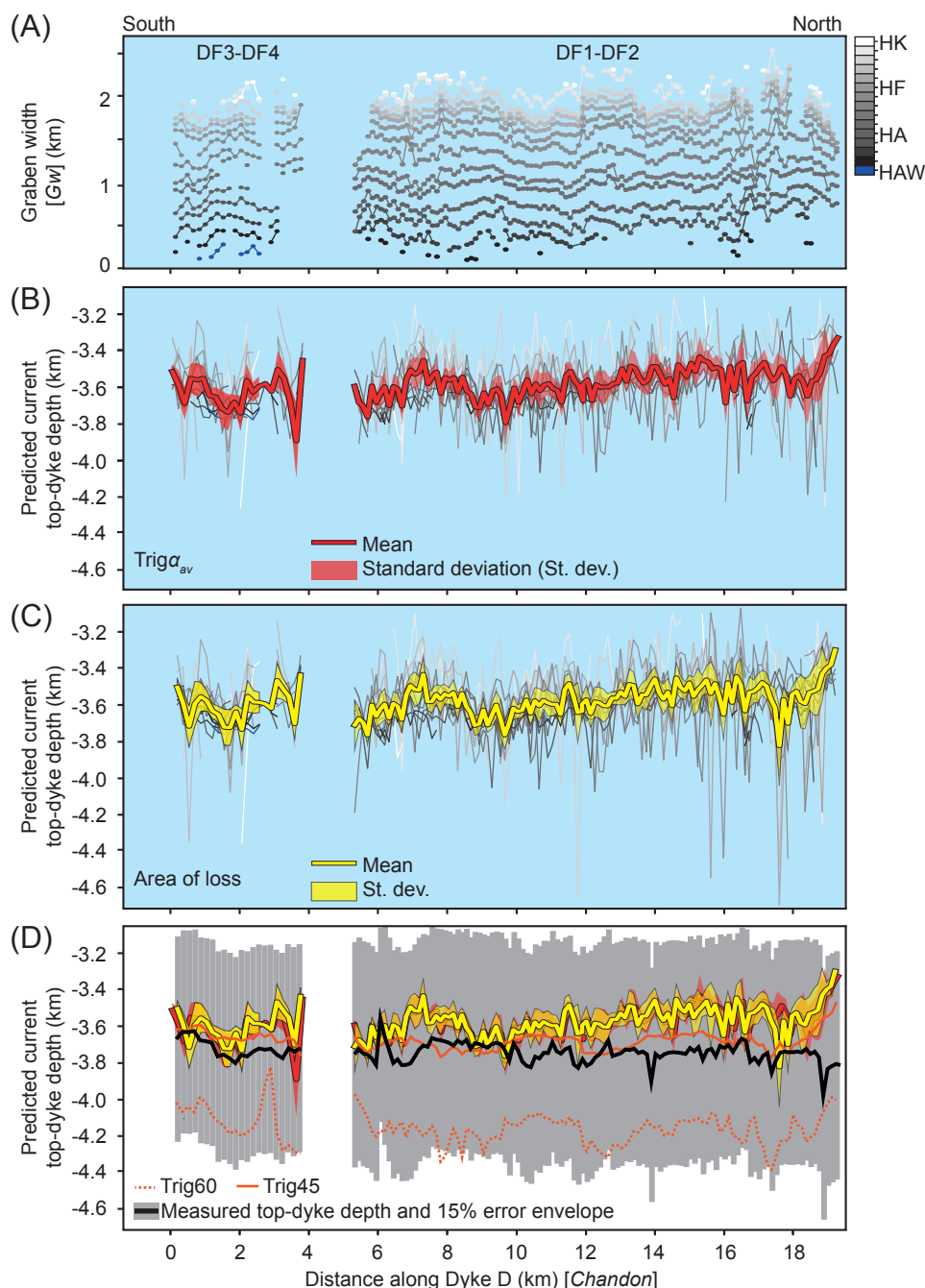


Figure 8 – (A) Graben width measurements for horizons HK–HAW above Dyke D in the Chandon 3D survey. Error bars not shown for clarity. (B) Top-dyke depths predicted using graben widths and average fault dips acquired from each horizon (HK–HAW) on each measurement transect. From the predicted top-dyke depths for all horizons, we calculate their mean and standard deviation. (C) Top-dyke depths predicted using the area of loss method and fault cut-offs mapped for each horizon (HK–HAW) on each measurement transect. From the predicted top-dyke depths for all horizons, we calculate their mean and standard deviation. (D) Plot comparing measured top-dyke depths with mean predicted top-dyke depths estimated using different methods (trig α_{av} , trig60, trig45, and area of loss). Standard deviation envelopes are shown for the trig α_{av} and area of loss methods.

4.4 Graben Widths and Predicted Top-Dyke Depths in 3D

To better evaluate the validity of top-dyke depth prediction methods, and extend the 3D analysis of DF1-DF2 and DF3-DF4 (Figure 8), we measured graben width across all mapped horizons above Dyke B in the Chandon 3D survey and Dyke E in the Chandon and Glencoe 3D surveys (all data provided in Magee et al., 2022; Magee and Love, 2021). The measured top-dyke depths beneath current sea-level range from

~3.3–3.7 km and ~3.3–3.6 km for dykes B and E, respectively (Figure 10A and B). Along the graben, over lateral distances of ~125–250 m, there are some abrupt changes of up to ~100 m in measured top-dyke depth superimposed onto broad increases and decreases of up to ~300 m over the kilometre-scale (Figure 10A and B). There is often scatter between the predicted top-dyke depths from different horizons, but mean values display relatively low (≤ 200 m) standard deviations, and those predictions derived from

Table 2 – Statistical F-tests comparing CM, VL, and KF data

Dyke-induced graben	Property	Interpreter	Mean (m)	Variance	F	F _{crit}
Dyke B, Chandon 3D survey	Horizontal graben width [G _W]	CM	1561	35490	1.31	1.49
		VL	1489	27083		
	Trig α_{av} estimated top-dyke depth	CM	3386	28122	1.65	1.49
		VL	3183	16996		
	Trig60 estimated current top-dyke depth	CM	4044	47071	1.14	1.49
		VL	3988	41204		
	Trig45 estimated current top-dyke depth	CM	3473	23542	1.08	1.49
		VL	3443	21842		
Area of loss estimated current top-dyke-depth	CM	3403	32538	2.05	1.49	
	VL	3198	15896			
Dyke E, Chandon 3D survey	Horizontal graben width [G _W]	CM	1120	30234	1.30	1.38
		VL	1102	39193		
	Trig α_{av} estimated top-dyke depth	CM	3379	17325	1.14	1.39
		VL	3205	19709		
	Trig60 estimated current top-dyke depth	CM	3818	23523	1.14	1.38
		VL	3803	26909		
	Trig45 estimated current top-dyke depth	CM	3408	09373	1.04	1.38
		VL	3400	09740		
Area of loss estimated current top-dyke-depth	CM	3389	17627	1.24	1.38	
	VL	3214	21813			
Dyke E, Glencoe 3D survey	Horizontal graben width [G _W]	KF	1303	34003	1.22	1.48
		VL	1321	27901		
	Trig α_{av} estimated top-dyke depth	KF	3520	21619	3.58	1.44
		VL	3618	77428		
	Trig60 estimated current top-dyke depth	KF	4056	26940	1.87	1.48
		VL	4031	14413		
	Trig45 estimated current top-dyke depth	KF	3579	10988	2.17	1.48
		VL	3548	05053		
Area of loss estimated current top-dyke-depth	KF	3509	19878	1.01	1.44	
	VL	3535	19741			

the trig α_{av} , trig45, and area of loss methods appear broadly comparable to measured top-dyke depths (Figure 10A and B). In contrast, top-dyke depths predicted using the trig60 method appear to overestimate dyke depths (Figure 10A and B). If we compare all top-dyke depth predictions, and not just derived means, those calculated using the trig α_{av} and area of loss methods are positively but weakly (R²=0.26 and 0.29) correlated to measured top-dyke depths; these methods have Root-Mean Square Errors (RSME) of ~180 m and seemingly tend to underestimate top-dyke depths (Figure 10C). The trig60 method is similarly positively but weakly (R²=0.29) correlated to measured top-dyke depths, but overestimates top-dyke depths and has an RSME of ~500 m (Figure 10C). Top-dyke depth predictions derived from the trig45 method display a moderate (R²=0.62), positive correlation with the measured top-dyke depths, and a RSME of ~100 m (Figure 10C).

4.5 Fault Displacement and Dip in 3D

We show how displacement varies along-strike and down-dip of all studied dyke-induced faults (Figure 11A) (all data provided in Magee et al., 2022; Magee and Love, 2021). Across these dyke-induced faults, displacement has a right-skew distribution but is ~26 m on average with a standard deviation of ~18 m

(Figure 10B). Displacement maxima rarely occur at fault upper or lower tips, with displacement typically higher towards fault centres (Figure 11A). Across EF1 and EF2 in the Chandon 3D survey, displacement gradually decreases northwards and is consistently greatest (up to ~101±15 m) on the W-dipping fault (EF2) where three, possibly four, zones of locally elevated displacement can be recognised (Figure 11A) (see also Magee and Jackson, 2021). There are no such zones of elevated displacement along EF1 (Figure 11A). In the Glencoe 3D survey, it is the E-dipping fault, EF3, which consistently has the greatest displacement (up to ~134±18 m) (Figure 10A). Yet EF3 shows no clear zones of elevated displacement, whereas EF4 can be sub-divided into at least three zones (Figure 11A). Where zones of elevated displacement occur along EF2 and EF4, they broadly appear to correlate with areas of higher fault dip (Figure 11). For the dyke-induced faults above dykes B and D, displacement gradually decreases northwards but there are no obvious zones of locally elevated displacement (Figure 11A). The dyke-induced faults above Dyke D have lower displacement (up to ~65±10 m) than those above dykes B (up to ~173±26 m) and E (Figure 11A). We also show dip varies along-strike and down-dip of all studied dyke-induced faults, although there are no systematic changes in its dis-

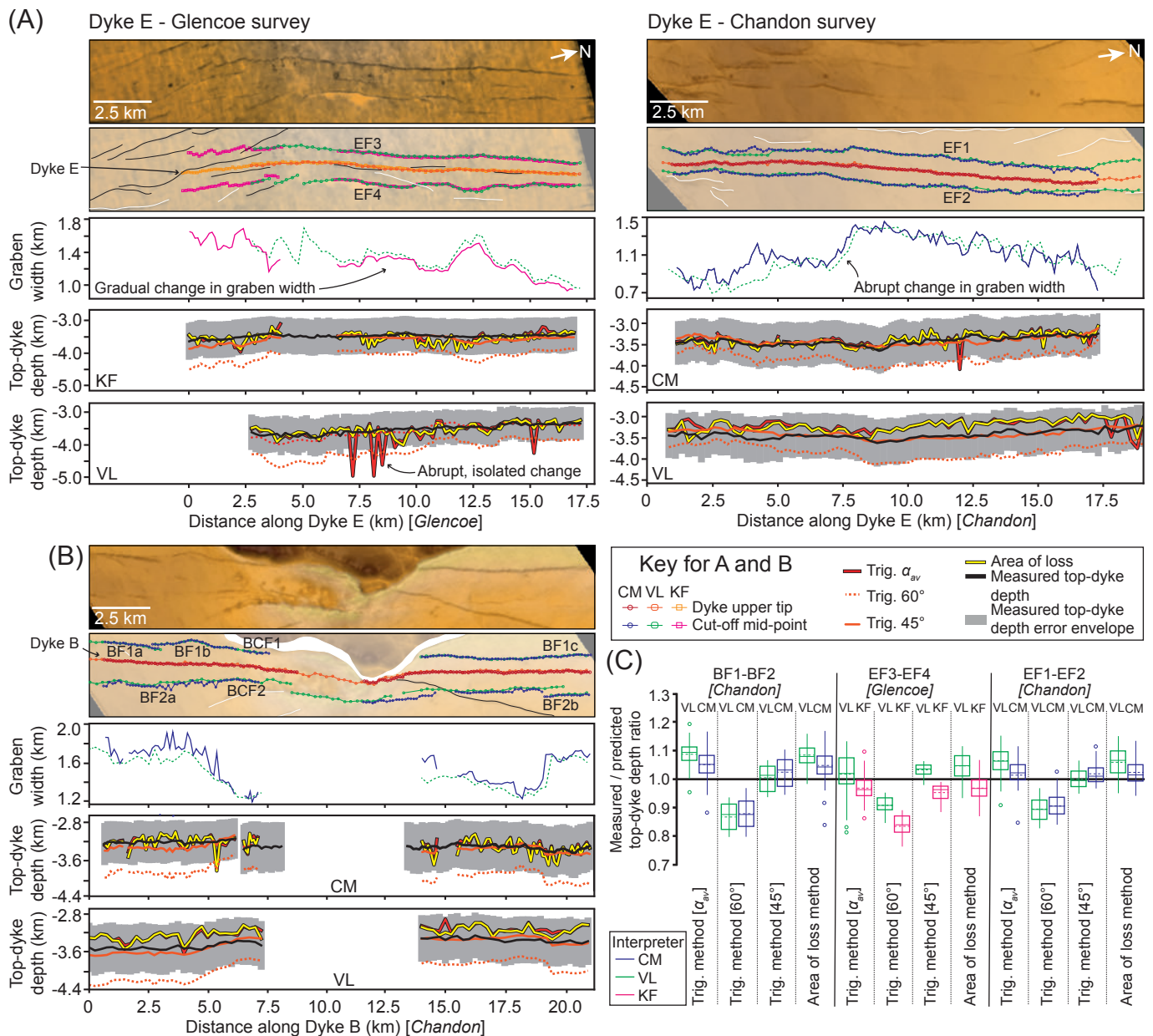


Figure 9 – (A-B) Uninterpreted and interpreted time-structure maps of the Top Mungaroo Formation (horizon HF) above dyke B and E in the Chandon and Glencoe 3D surveys (see Figure 3C for key and locations). Footwall cut-off and dyke upper tip depth locations mapped by different interpreters are shown. Plots compare graben width, average fault dip, and cumulative displacement (displ.) calculated from different interpreters' cut-off mapping. Also shown are plots comparing measured top-dyke depths with those predicted using different methods (trig α_{av} , trig60, trig45, and area of loss). Error bars are not shown because we compare calculations subject to the same uncertainties and to improve clarity; we make an exception for the measured top-dyke depths, for which we include a $\pm 15\%$ error envelope, to enable a broader comparison to predicted top-dyke depths. Data for Dyke B in the Glencoe survey shown in Figure SI-3, in Supporting Information. **(C)** Box-and-whisker plots comparing measured and predicted top-dyke depths ratios calculated by different methods and using fault cut-off datasets mapped by different interpreters. The boxes describe the interquartile range and median of each dataset, with the whiskers marking lower and upper extremes of the data. We also show the mean (dashed line) and outliers in these data.

tribution (Figure 11C). Average fault dips, calculated from the dips of both opposing dyke-induced faults on each transect at each horizon, are normally distributed with a mean of 41° and standard deviation of 7.5° (Figure 11D).

5 Discussion

5.1 Interpretation Bias

The studied dyke-induced faults have relatively low displacements (>75 m, with an average of ~ 26 m; Figure 11B). Given the vertical ($\sim 20 \pm 4$ m) and horizontal (~ 25 m) resolution limits of the seismic reflection data used, these low displacements mean many portions of the dyke-induced faults are not imaged as clear off-sets in reflections (e.g., Figure 5B). Instead, the dyke-

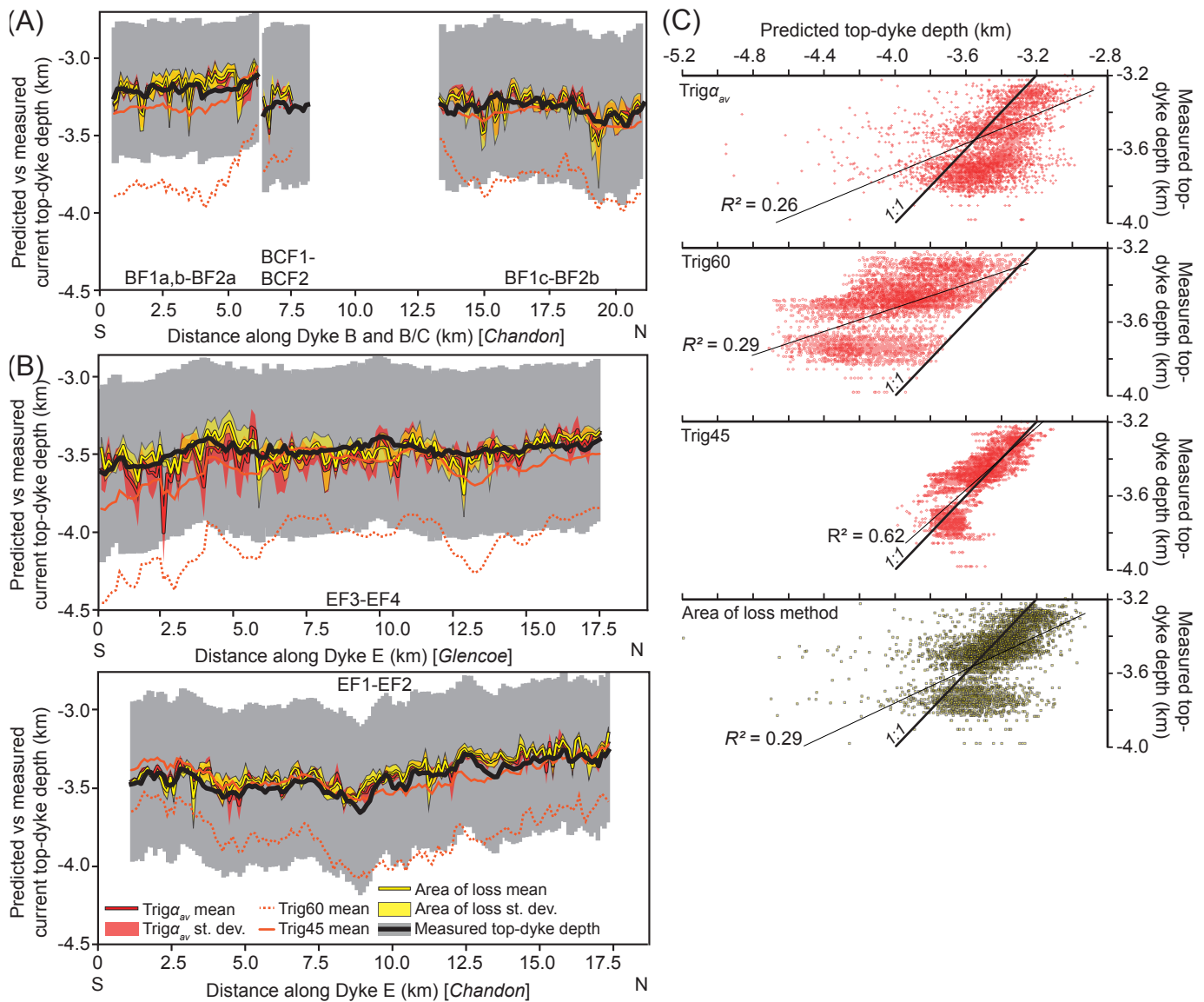


Figure 10 – (A-B) Plots comparing measured top-dyke depths with mean predicted top-dyke depths estimated from all horizons using different methods (trig α_{av} , trig60, trig45, and area of loss) for dykes B and E in the Chandon and Glencoe 3D surveys. Standard deviation envelopes are shown for the trig α_{av} and area of loss methods, and the error envelope (grey) of the measured top-dyke depths is $\pm 15\%$. **(C)** All measured top-dyke depths compared to predicted top-dyke depths estimated from the trig α_{av} , trig60, trig45, and area of loss methods used.

induced faults often correspond to areas where seismic reflections are subtly distorted and appear folded (e.g., Figures 3A, B, and 5D). In such a situation, a dyke-induced fault may extend through the distorted reflections, but the interpreter has to decide whether the fault intersects the middle of the rotated reflection limb, either of its inflection points, or elsewhere (e.g., Figure 5D) (e.g., *Faleide et al., 2021*). It is also plausible that the distorted reflections correspond to folded strata, perhaps generated by fault propagation folding above a buried fault tip, and there is no fault present at that stratigraphic level at all. These uncertainties, associated with mapping fault cut-offs, affect all quantitative fault measurements (e.g., displacement and graben width) (e.g., *Alcalde et al., 2017a; Faleide et al., 2021*). In their quantitative dyke-induced fault study, (*Magee and Jackson, 2021*) assumed this interpreter bias could be accounted for by considering measured or calculated fault proper-

ties had errors of $\pm 5\%$.

In our study, where the same fault cut-off sets were mapped by the same author, but at a different time (i.e. CM1 and CM2), variations in average dip and cumulative displacement occur due to supposedly coincident fault cut-offs being mapped up to ~ 100 m away along the transect (~ 18 m on average) (Table SI-3, in Supporting Information). These distances have the same order of magnitude as fault heave and throw, and therefore significantly affect calculated dips and displacements. Conversely, the ± 100 m differences in fault cut-off position are much less than, and thus have little impact on graben widths, which are typically > 1500 m (Table SI-2, In Supporting Information). Despite differences in observed cut off position, fault properties extracted from CM1 and CM2 show little variance and can be considered similar (Table 1). Top-dyke depths predicted from both datasets us-

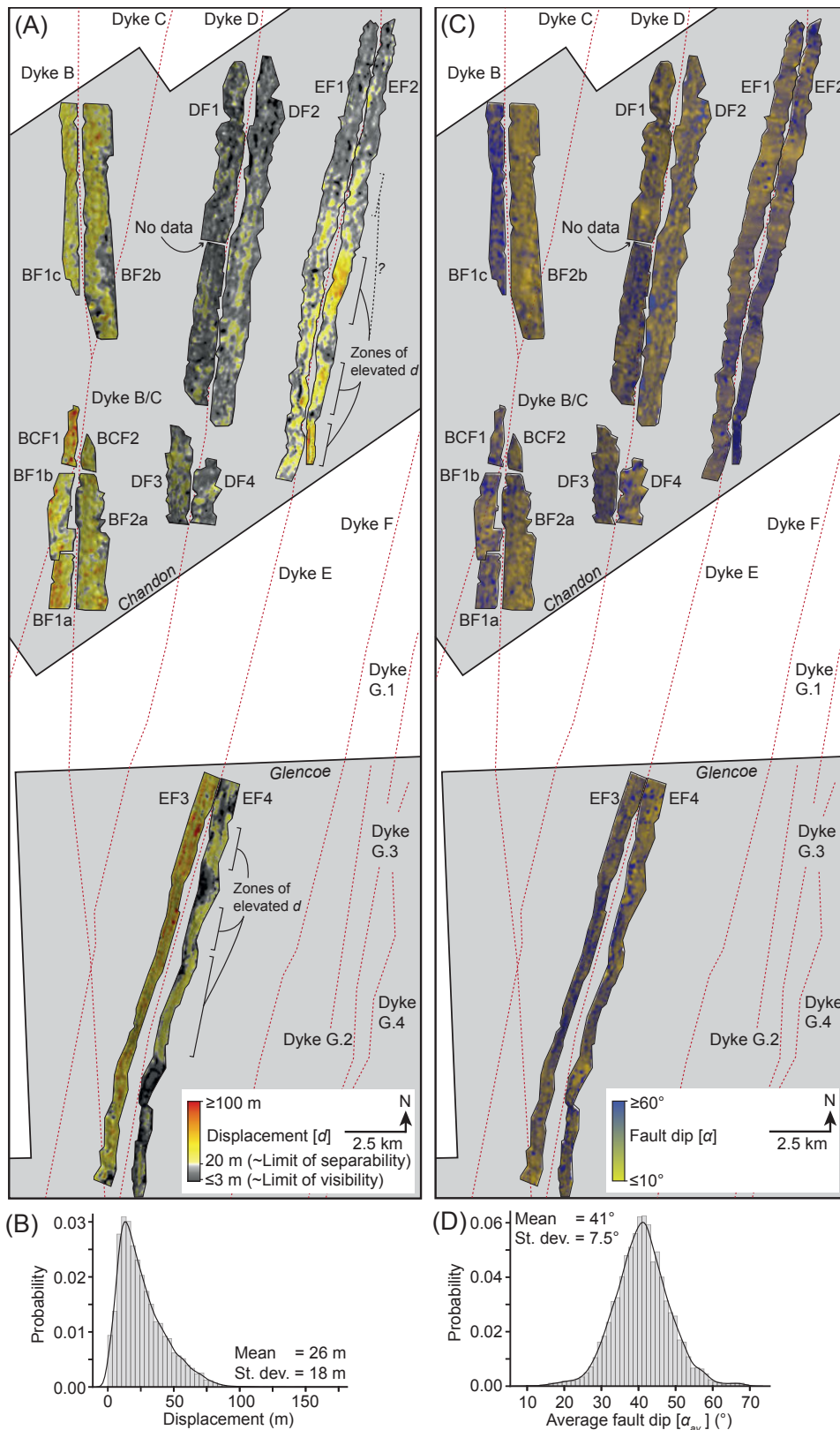


Figure 11 – (A) Fault displacement maps across the Chandon (top) and Glencoe (bottom) 3D surveys (see Magee and Jackson, 2020, for method). Dyke traces also shown (Magee and Jackson, 2021). We project displacement data onto fault surfaces at X, Y, and Z coordinates marking the mid-point between each paired footwall and hanging wall cut-off (Figure 4A); a convergent interpolation gridding algorithm was used to linearly extrapolate between data points and preserve any trends. (B) Probability density function plot of measured fault displacements, showing they have a right-skewed distribution. (C) Fault dip (α) maps (see Magee and Jackson, 2020, for method). Dyke traces also shown (Magee and Jackson, 2021). Fault dip maps may contain interpolation errors derived from our choice gridding algorithms, but we consider these negligible given the high density of measurement locations across both faults. (D) Probability density function plot of measured average fault dips (α_{av}), showing they have a normal distribution.

ing trigonometry methods are also statistically similar, but those predicted using the area of loss method are not (Table 1). Our data thus suggest that although an individual interpreter may introduce bias into their fault cut-off mapping, their findings are generally consistent. Such 'internal consistency' from geologists has been observed for several data types, including the characterisation of faults and fractures (Andrews et al., 2019; Shipton et al., 2020) and models built from seismic reflection datasets (Alcalde and Bond, 2022); this is likely a result of the conceptual model(s) of the interpreter (i.e. the simplified internal representation of the process or problem being assessed) (e.g., Gibson et al., 2016; Shipley and Tikoff, 2016). These conceptual models are influenced by the cognitive style and experience of the interpreter (Bond et al., 2007; Shipley and Tikoff, 2016), as well as the purpose and time constraints associated with data collection and quality control (e.g., Andrews et al., 2019; Shipton et al., 2020).

We find that where fault properties and predicted top-dyke depths are derived from fault cut-offs mapped by different authors, their values are broadly similar and the same profile patterns along the graben length are reproduced (Figures 6 and 8). Our statistical F-test shows that, in some instances, fault properties and predicted top-dyke depths from these datasets can be considered similar, but not always (Tables 1 and 2). There are many potential reasons why data derived from different interpreters is variable, including: (1) seismic reflection data quality (Alcalde et al., 2017a,b; Faleide et al., 2021); (2) interpreter experience (Bond et al., 2007, 2015); (3) applied methods of mapping (e.g., were seismic attributes used to constrain interpretations?) (Ranky and Mitchell, 2003); (4) the vertical exaggeration and scale used during fault picking (Alcalde et al., 2019); and (5) the time available to collect and quality check the dataset (e.g., Bond et al., 2007, 2015; Faleide et al., 2021; Macrae et al., 2016). Previous work has shown that variance between interpreters can be reduced where a pre-interpretation picking strategy was implemented, training material was used by all interpreters prior to picking, and/or an element of group working or training is employed (see Alcalde and Bond, 2022, and references therein). Overall, our data suggest that the arbitrary $\pm 5\%$ error applied by Magee and Jackson (2020) may be insufficient to describe extracted fault properties, with errors of $\gg 5\%$ observed. Until a more detailed parametric study can be carried out, we suggest that arbitrary but conservative errors of $\pm 10\%$ are used, particularly where fault displacement is close to or below the separation limit of the dataset. Such an increase in error would not significantly affect the displacement (and heave) patterns mapped by Magee and Jackson (2021), implying their inferences on fault growth and the utility of surface heave as a proxy for dyke thickness remain valid interpretations. However, we note that accounting for $\pm 10\%$ errors will reduce the potential discrepancy between their top-dyke depths measured from the data

and estimated from graben width (Magee and Jackson, 2021).

5.2 Predicting Top-Dyke Depths from Dyke-induced Fault Surface Expressions

Our data enable us to examine how predicted top-dyke depths, estimated using several methods, compare to measured depths. For example, we test the predictive power of the trigonometry method using an average of the measured faults dips ($\text{trig}\alpha_{\text{av}}$), which varies on each transect, compared to where fault dip is assumed constant (at 60° or 45°). We show that predictions of top-dyke depths made using graben width, fault dip, and/or displacement measurements are typically within error of measured top-dyke depths (Figures 6-10). Despite these similarities, predictions made using the $\text{trig}\alpha_{\text{av}}$ and area of loss methods typically underestimate top-dyke depths and display only a weak, positive relationship to measured top-dyke depths ($R^2 = 0.26$ and 0.29 , respectively) (Figure 11C). These discrepancies and weak correlation between $\text{trig}\alpha_{\text{av}}$ and area of loss method predictions and measured top-dyke depths relate to the incorporation of measured, as opposed to assumed, fault dip data. Fault dip measurements are susceptible to interpretation bias and vary across the fault plane over short (100–200 m) length-scales (Figure 11C). Projection of a fault with such variations in dip may thus be best achieved by using a constant dip representative of the entire fault. Although assuming dyke-induced faults dip consistently at 60° leads to overestimates of top-dyke depths, our data do show that assuming a consistent dip of 45° provides a good fit between predicted and measured top-dyke depths, likely because it is similar to the mean (41°) of all fault dip measurements (Figure 10D and 11D). Our data support previous studies that use constant fault dips to predict top-dyke depths (e.g., Hjartardóttir et al., 2016), implying we can relate the surface expression of dyke-induced faults, at least to some extent, to underlying dyke geometry (cf. Magee and Jackson, 2021). However, we note that without 3D imaging of dyke-induced fault planes, we cannot ascertain whether the average of fault dips measured at a single surface or horizon, or an assumed fault dip (e.g., 60° or 45°), are representative of its dip variations with depth. For example, if fault dips continuously decrease with depth, such that the faults are concave-upwards, assuming fault dip is constant will result in overestimating top-dyke depths (Magee and Jackson, 2021).

The dyke upper tips we study are currently located ~ 3.3 – 3.8 km below sea-level (Figures 6-10), and extended upwards to depths of at least ~ 1 km when they were intruded, assuming horizon HK marks the syn-emplacement free surface (Magee and Jackson, 2020, 2021). Both our measurements and predictions suggest top-dyke depths vary along-strike by several hundred metres, with changes either being abrupt or gradual over several kilometres (Figures 6-10). Abrupt changes in along-strike top-dyke depths are

within error, and so they could be an artefact of our interpretation (Figures 6-10). However, dykes B and E, and to a lesser extent Dyke D, show systematic increases and decreases in upper tip depth of up to ~300 m, which is above expected error, with wavelengths of several kilometres (Figures 6-10); similar fluctuations in top-dyke tip depth, albeit on length scales of 10's of kilometres, have been shown for other members of the Exmouth Dyke Swarm (Magee and Jackson, 2020) and for dykes in Elysium Fossae, Mars (Rivas-Dorado et al., 2021). Kilometre-scale, along-strike variations in top-dyke depth have been observed in recent dyking episodes (e.g., Ágústsdóttir et al., 2016; Trippanera et al., 2019; Xu et al., 2016), and may be a common feature of dyke swarms (e.g., Magee and Jackson, 2020; Rivas-Dorado et al., 2021).

There are several reasons why the upper tip depth of laterally propagating dykes may increase and decrease along-strike. For example, a head region may develop at the propagating edge of a dyke, which is taller and reaches a shallower level than the tail (Figure 12A and B) (e.g., Rivalta et al., 2015; Rivas-Dorado et al., 2021). If the seismic expression of the intrusions corresponds to multiple, adjacent dykes (Magee and Jackson, 2020), differences in the distance each dyke propagated could cause top-dyke depths to vary beneath the graben (Figure 12A) (Rivas-Dorado et al., 2021). Alternatively, propagation of a dyke (with or without a head) may have stalled, leading to its crystallisation and pressurisation until magma broke out from the dyke 'nose' to form a new segment that grew laterally and vertically (Figure 12B) (Healy et al., 2018; Magee and Jackson, 2021). A transition to vertical or inclined magma flow towards dyke tops can also cause dyke upper tips to segment and locally propagate vertically, affecting dyke height (e.g., Poland et al., 2008). Such dyke segmentation can particularly occur when emplacement occurs beneath a volcano load (Figure 12C) (e.g., Poland et al., 2008), as the sloping topography results in changes to the lithostatic stresses above and along underlying dykes (Urbani et al., 2017). Density layering in the host rock is another relevant factor that controls the vertical stability of dykes, and therefore their depths; stratified host rocks are more likely to contain dykes with smaller vertical extents, which are stable under a wider range of conditions (Pollard and Townsend, 2018). Lateral changes in the vertical stratigraphic sequence may thus control how close to the free surface a dyke may reach. Finally, increases or decreases in magma density may cause dyke upper tips to become unstable and adjust to a new structural levels (Figure 12D) (e.g., Townsend et al., 2017). Regardless of the driving mechanism, areas where top-dyke depths become shallower may focus magma flow and promote local upwards propagation, potentially leading to and explaining the restricted distribution of fissure eruptions along dyke lengths (e.g. Pansino et al., 2019; Woods et al., 2019).

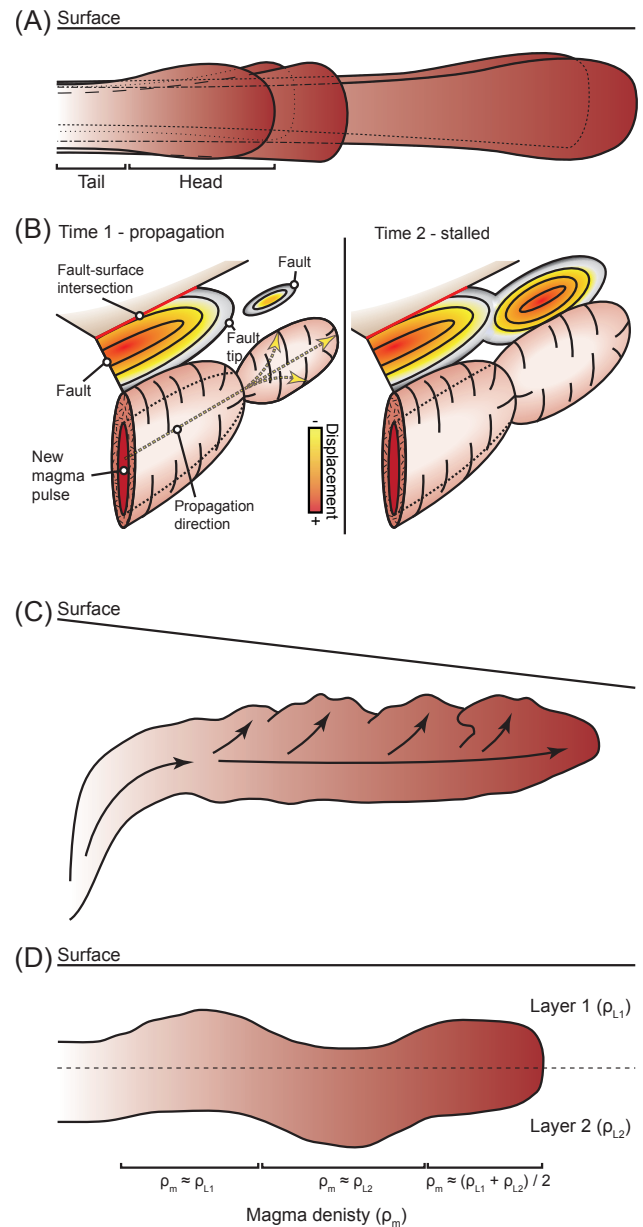


Figure 12 – Possible mechanisms for changing top-dyke depths along-strike. **(A)** Laterally propagating dykes develop a head region that is taller and extends to shallower levels than the tail behind (modified from Rivas-Dorado et al., 2021). **(B)** Cyclical stalling and propagation of the dyke leads to magma breaking out from the dyke 'nose', where it is vertically restricted (Magee and Jackson, 2020). **(C)** Under a variable volcano load, the ascent and lateral propagation of a dyke results in segmentation of its upper tip, which locally focuses magma flow and drives upward propagation (modified from Poland et al., 2008). **(D)** Changes in magma density, relative to that of a host rock displaying a density stratification, can cause the upper and lower tip positions of a propagating dyke to destabilize and transgress upwards or downwards (Townsend et al., 2017). Where the magma density is equal to the average of two host rock layers of different densities, the dyke upper and lower tips are equally spaced from the layer boundary (Townsend et al., 2017). If magma density changes (e.g., through vesiculation, crystallisation, and/or cooling) and becomes closer in density to one of the layer, it will preferentially intrude within that layer, causing the upper and lower tips to move (Townsend et al., 2017).

5.3 Dyke-Induced Fault Growth and Kinematics

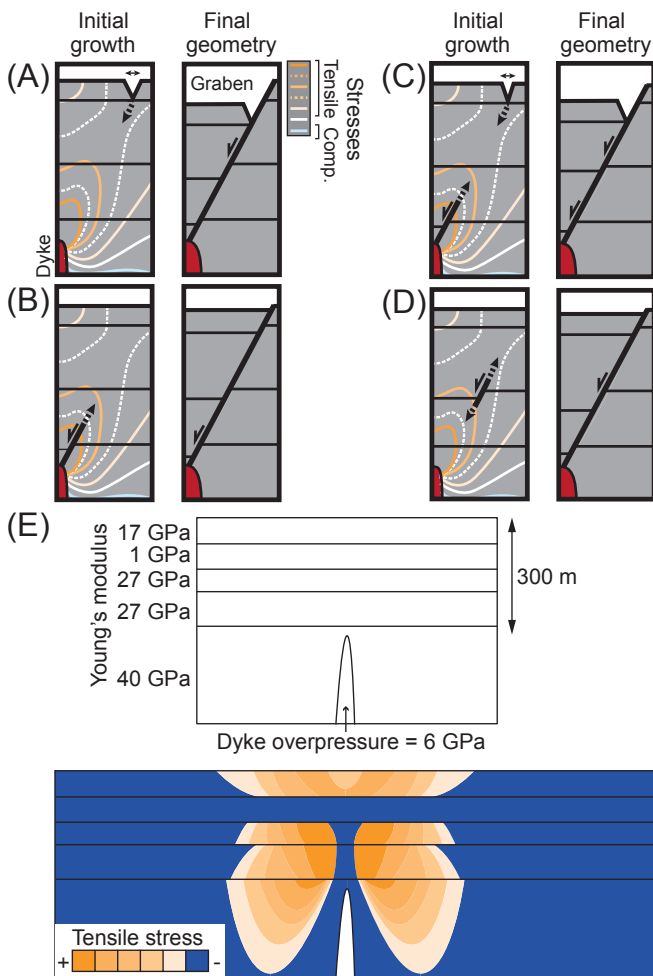


Figure 13 – (A–D) Dyke-induced fault growth models (based on Koehn et al., 2019; Magee and Jackson, 2020; Mastin and Pollard, 1988; Rubin and Pollard, 1988; Tentler, 2005; Trippanera et al., 2015b). Horizontal stress patterns above an intruding dyke in a homogeneous elastic medium, showing tensile stress is concentrated at the surface and above the dyke tip (redrawn from Rubin and Pollard, 1988). (E) Numerical model of tensile stresses above a dyke arrested at 300 m below the surface, with an overpressure of 6 GPa, in a layered medium (redrawn from Al Shehri and Gudmundsson, 2018, their Fig. 21). Tensile stresses are concentrated above the dyke tip and in two zones at the surface, but the presence of layering disrupts its distribution; e.g., the weak layer, which has a Young's modulus of 1 GPa, suppresses stress concentration (Al Shehri and Gudmundsson, 2018).

Field- and geophysical-based observations, coupled with physical, analytical, and numerical models suggest dyke-induced faults probably nucleate either: (1) near the surface, initiating as vertical tensile fractures that propagate downwards and develop into shear fractures (Figure 13A) (e.g., Al Shehri and Gudmundsson, 2018; Trippanera et al., 2015a,b; von Hagke et al., 2019); (2) as shear fractures that grow upwards from dyke upper tips (Figure 13B) (e.g., Koehn et al., 2019; Rubin, 1992; Xu et al., 2016); (3) at both the surface and dyke upper tip, linking as they propagate downwards and upwards, respectively (Figure 13C)

(Rowland et al., 2007; Tentler, 2005); or (4) between the surface and dyke tip, propagating both upwards and downwards (Figure 13D) (Koehn et al., 2019; Magee and Jackson, 2021; Mastin and Pollard, 1988).

If we expect displacement to be greatest where faults nucleate (e.g., Pollard and Segall, 1987; Trippanera et al., 2015b), our mapped displacement distributions suggest fault segments initially developed between the dyke upper tip and coeval free surface (Figure 10A and C) (Koehn et al., 2019; Magee and Jackson, 2021; Mastin and Pollard, 1988). Yet dyke opening induces tensile stresses in the overburden, focused at the dykes upper tip and in two zones at the free surface, where modelling suggest fault nucleation most likely to occur (Figure 1A) (e.g., Koehn et al., 2019; Pollard et al., 1983; Rubin, 1992; Rubin and Pollard, 1988). However, these models assume dyke intrusion occurs within a homogenous, elastic half-space (e.g., Koehn et al., 2019; Pollard et al., 1983; Rubin, 1992; Rubin and Pollard, 1988). Where mechanical layers with different physical properties are modelled above dykes, tensile stresses have been shown to become concentrated in relatively strong units away from the dyke tip or free surface (Figure 13E) (Al Shehri and Gudmundsson, 2018). The dyke-induced faults we analyse primarily offset heterolithic fluvio-deltaic rocks (e.g., Bilal et al., 2018; Martin et al., 2018), as well as Jurassic sandstones and claystones (Figures 2B, 3A and B) (Tindale et al., 1988). The layered sedimentary succession offset by the dyke-induced faults is thus likely mechanically heterogeneous, which could have affected stress distribution and fault nucleation during dyking (Al Shehri and Gudmundsson, 2018; Schöpfer et al., 2006, e.g.). Alternatively, displacement may preferentially accrue on faults away from their nucleation site if post-emplacment dyke thickening instigated slip (Magee and Jackson, 2021); in this scenario, displacement maxima may develop along faults away from their nucleation sites, meaning displacement distribution cannot be used to reconstruct dyke-induced fault kinematics.

6 Conclusions

Dyke-induced faults are common in many volcanic settings on Earth and other planetary bodies (e.g., Mars). Because we often have no or little access to the subsurface in these locations, relating the surface expression of dyke-induced faults to the underlying dyke geometry can provide key insight into the 3D structure of and processes active during dyke emplacement. However, deriving dyke geometry from the surface expression of dyke-induced faults is only feasible if the faults project straight down-dip to the dyke upper tip. Yet recent analysis of 3D seismic reflection imagery suggests dyke-induced faults are non-planar. We show that interpretation bias does introduce uncertainty into the quantitative analysis of dyke-induced faults using seismic reflection data, but that we can still use these data to confidently understand dyke and dyke-induced fault structure in 3D.

By quantitatively measuring dyke-induced fault and graben geometries, we demonstrate that: (1) predictions of top-dyke depths are typically within error of measured top-dyke depths, but most accurate when incorporating information on the average dip of entire faults; and (2) dyke-induced fault displacement and dip are variable along-strike and down-dip. Our work supports previous findings and relates dyke-induced faulting to the nucleation of isolated fault segments above propagating dyke segments, which linked as they grew in response to dyke stalling and thickening. Cyclical dyke propagation and stalling, or other processes leading to the emplacement of dyke segments, may also explain the hectometre-scale variation in dyke upper tip depths we observe along dyke strike. Overall, our work suggests that we can relate the surface expression of dyke-induced faults to subsurface dyke geometry, but only if we have some information on the 3D structure of the faults. Reflection seismology is a critical tool for developing our understanding of dyke-induced faulting.

Acknowledgements

CM is grateful to funding from a NERC Independent Research Fellowship (NE/R014086/1) and to Geoscience Australia for making all seismic reflection and borehole datasets publically available. We also acknowledge Schlumberger for provision of the seismic interpretation software Petrel and Dug Insight for the provision of the seismic interpretation software. We thank Renata da Silva Schmitt for editorial handling, and Natasha Stanton and Juan Alcalde for their thorough, constructive reviews.

Author contributions

CM conceived and designed the work, acquired the data, contributed to data analysis and interpretation, and wrote the manuscript. Both **VL** and **KF** were involved in project design and data analysis, and proof-read the manuscript. **BA**, **SR-D**, **CO**, **CJ**, and **EB** were involved in data analysis and interpretation, and critically revised the manuscript.

Data availability

Seismic reflection and borehole data used in this study are freely available from either the Geoscience Australia NOPIMS (<https://nopims.dmp.wa.gov.au/nopims>) data repository or that of the UK National Geoscience Data Centre (NGDC; <https://www.bgs.ac.uk/geological-data/national-geoscience-data-centre/>). The NOPIMS data access centre allows “Wells” (i.e., for this study Chandon-1, Chandon-2, Chandon-3, Yellowglen 1, Briseis-1, Dunlop-1, Elfin-1, Glencoe-1, and Toporoa-1) and “Surveys” (i.e., for this study the Chandon 3D MSS and Glencoe 3D seismic reflection surveys) from offshore Australia to be searched for. From these search results, borehole data can be downloaded

by highlighting the correct borehole and using “view details for selected rows”; due to the file size of 3D seismic reflection segy data, few can be downloaded but all can be added to a basket and requested from Geoscience Australia. These data can also be downloaded from the NGDC under the title “3D seismic reflection surveys (Chandon and Glencoe) and borehole data from offshore NW Australia.” All measurements and calculations acquired during this research, as well as mapped seismic horizons, are provided as Supporting Information (available at Figures SI-1, SI-2, and SI-3; Table SI-1; Table SI-2; and Table SI-3) or hosted by the NGDC (Magee et al., 2022; Magee and Love, 2021).

Competing interests

The authors declare no competing interests.

Peer review

This publication was peer-reviewed by Juan Alcalde and Natasha Stanton. The full peer-review report can be found here: <https://tektonika.online/index.php/home/article/view/25/30>

Copyright notice

© Author(s) 2023. This article is distributed under the Creative Commons Attribution 4.0 International License, which permits unrestricted use, distribution, and reproduction in any medium, provided the original author(s) and source are credited, and any changes made are indicated.

References

- Ágústsdóttir, T., J. Woods, T. Greenfield, R. G. Green, R. S. White, T. Winder, B. Brandsdóttir, S. Steinhórsón, and H. Soosalu (2016), Strike-slip faulting during the 2014 Bárðarbunga-Holuhraun dike intrusion, central Iceland, *Geophysical research letters*, 43(4), 1495–1503, doi: 10.1002/2015gl067423.
- Al Shehri, A., and A. Gudmundsson (2018), Modelling of surface stresses and fracturing during dyke emplacement: Application to the 2009 episode at harrat lunayyir, Saudi Arabia, *Journal of Volcanology and Geothermal Research*, 356, 278–303, doi: 10.1016/j.jvolgeores.2018.03.011.
- Alcalde, J., and C. E. Bond (2022), Chapter 5 - subjective uncertainty and biases: The impact on seismic data interpretation, in *Interpreting Subsurface Seismic Data*, edited by R. Bell, D. Iacopini, and M. Vardy, pp. 103–123, Elsevier, doi: 10.1016/B978-0-12-818562-9.00002-9.
- Alcalde, J., C. E. Bond, G. Johnson, J. F. Ellis, and R. W. H. Butler (2017a), Impact of seismic image quality on fault interpretation uncertainty, *GSA today: a publication of the Geological Society of America*, doi: 10.1130/gsatg282a.1.
- Alcalde, J., C. E. Bond, and C. H. Randle (2017b), Framing bias: The effect of figure presentation on seismic interpretation, *Interpretation*, 5(4), T591–T605, doi: 10.1190/int-2017-0083.1.

- Alcalde, J., C. E. Bond, G. Johnson, A. Kloppenburg, O. Ferrer, R. Bell, and P. Ayarza (2019), Fault interpretation in seismic reflection data: an experiment analysing the impact of conceptual model anchoring and vertical exaggeration, *Solid earth*, 10(5), 1651–1662, doi: 10.5194/se-10-1651-2019.
- Allen, P. A., and J. R. Allen (2013), *Basin Analysis: Principles and Application to Petroleum Play Assessment*, John Wiley & Sons.
- Anderson, E. M. (1951), *The dynamics of faulting and dyke formation with applications to Britain*, 206 pp., Hafner Pub. Co., Edinburgh.
- Andrews, B. J., J. J. Roberts, Z. K. Sipton, S. Bigi, M. C. Tartarello, and G. O. Johnson (2019), How do we see fractures? quantifying subjective bias in fracture data collection, *Solid earth discussions*, 10(2), 1–44, doi: 10.5194/se-2018-135.
- Bilal, A., and K. McClay (2022), Tectonic and stratigraphic evolution of the central exmouth plateau, NW shelf of australia, *Marine and Petroleum Geology*, 136(105447), 105,447, doi: 10.1016/j.marpetgeo.2021.105447.
- Bilal, A., K. McClay, and N. Scarselli (2018), Fault-scarp degradation in the central exmouth plateau, north west shelf, australia, *Geological Society special publication*, 476, SP476. 11.
- Black, M., K. D. McCormack, C. Elders, and D. Robertson (2017), Extensional fault evolution within the exmouth sub-basin, north west shelf, australia, *Marine and Petroleum Geology*, 85, 301–315, doi: 10.1016/j.marpetgeo.2017.05.022.
- Bond, C. E., A. D. Gibbs, Z. K. Sipton, and S. Jones (2007), What do you think this is? ‘conceptual uncertainty’ in geoscience interpretation, *GSA today: a publication of the Geological Society of America*, 17(11), 4–10.
- Bond, C. E., G. Johnson, and J. F. Ellis (2015), Structural model creation: the impact of data type and creative space on geological reasoning and interpretation, *Geological Society special publication*, 421(1), 83–97.
- Bosworth, W., D. F. Stockli, and D. E. Helgeson (2015), Integrated outcrop, 3D seismic, and geochronologic interpretation of red sea dike-related deformation in the western desert, Egypt-The role of the 23ma cairo “mini-plume”, *Journal of African Earth Sciences*, 109, 107–119.
- Brown, A. R. (2011), *Interpretation of three-dimensional seismic data, AAPG Memoir 42, SEG Investigations in Geophysics No. 9*, vol. 42, 6th ed., 534 pp., American Association of Petroleum Geologists, Oklahoma, USA, doi: 10.1306/m4271346.
- Delogkos, E., T. Manzocchi, C. Childs, C. Sachanidis, T. Barbas, M. P. J. Schöpfer, A. Chatzipetros, S. Pavlides, and J. J. Walsh (2017), Throw partitioning across normal fault zones in the ptolemais basin, greece, *Geological Society special publication*, 439(1), 333–353.
- Dimmen, V., A. Rotevatn, and I. Lecomte (2023), Imaging of small-scale faults in seismic reflection data: Insights from seismic modelling of faults in outcrop, *Marine and Petroleum Geology*, 147(105980), 105,980, doi: 10.1016/j.marpetgeo.2022.105980.
- Direen, N. G., H. M. J. Stagg, P. A. Symonds, and J. B. Colwell (2008), Architecture of volcanic rifted margins: new insights from the exmouth – gascoyne margin, western australia, *Australian Journal of Earth Sciences*, 55(3), 341–363, doi: 10.1080/08120090701769472.
- Drymoni, K., E. Russo, A. Tibaldi, N. Corti, F. L. Bonali, and F. P. Mariotto (2023), Dyke-induced graben formation in a heterogeneous succession on mt. etna: Insights from field observations and FEM numerical models, *Journal of Volcanology and Geothermal Research*, 433(107712), 107,712, doi: 10.1016/j.jvolgeores.2022.107712.
- Dumont, S., A. Socquet, R. Grandin, C. Doubre, and Y. Klinger (2015), Surface displacements on faults triggered by slow magma transfers between dyke injections in the 2005–2010 rifting episode at Dabbahu-Manda-Hararo rift (afar, ethiopia), *Geophysical Journal International*, 204(1), 399–417, doi: 10.1093/gji/ggv449.
- Dumont, S., Y. Klinger, A. Socquet, C. Doubre, and E. Jacques (2017), Magma influence on propagation of normal faults: Evidence from cumulative slip profiles along Dabbahu-Manda-Hararo rift segment (afar, ethiopia), *Journal of Structural Geology*, 95, 48–59, doi: 10.1016/j.jsg.2016.12.008.
- Exon, N. F., B. U. Haq, and U. Von Rad (1992), Exmouth plateau revisited: scientific drilling and geological framework, in *Proceedings of the Ocean Drilling Program, Scientific Results*, vol. 122, pp. 3–20.
- Faleide, T. S., A. Braathen, I. Lecomte, M. J. Mulrooney, I. Midtkandal, A. J. Bugge, and S. Planke (2021), Impacts of seismic resolution on fault interpretation: Insights from seismic modelling, *Tectonophysics*, 816(229008), 229,008, doi: 10.1016/j.tecto.2021.229008.
- Gartrell, A., J. Torres, M. Dixon, and M. Keep (2016), Mesozoic rift onset and its impact on the sequence stratigraphic architecture of the northern carnarvon basin, *The APPEA journal*, 56(1), 143, doi: 10.1071/aj15012.
- Gibson, H., I. S. Stewart, S. Pahl, and A. Stokes (2016), A “mental models” approach to the communication of sub-surface hydrology and hazards, *Hydrology and Earth System Sciences*, 20(5), 1737–1749, doi: 10.5194/hess-20-1737-2016.
- Hardy, S. (2016), Does shallow dike intrusion and widening remain a possible mechanism for graben formation on mars?, *Geology*, 44(2), 107–110, doi: 10.1130/g37285.1.
- Healy, D., R. E. Rizzo, M. Duffy, N. J. C. Farrell, M. J. Hole, and D. Muirhead (2018), Field evidence for the lateral emplacement of igneous dykes: Implications for 3D mechanical models and the plumbing beneath fissure eruptions, *Volcanica*, 1(2), 85–105, doi: 10.30909/vol.01.02.85105.
- Hjartardóttir, Á. R., P. Einarsson, M. T. Gudmundsson, and T. Högnadóttir (2016), Fracture movements and graben subsidence during the 2014 bárðarbunga dike intrusion in iceland, *Journal of Volcanology and Geothermal Research*, 310, 242–252, doi: 10.1016/j.jvolgeores.2015.12.002.
- Hocking, R. M., W. J. E. Van de Graaff, H. T. Moors, and G. S. of Western Australia. (1987), *Geology of the Carnarvon Basin, Western Australia / by R.M. Hocking, H.T. Moors and W.J.E. Van de Graaff*, xiv, 288, [1] p. : pp., Geological Survey of Western Australia Perth, W.A.
- Hofmann, B. (2013), *How do faults grow in magmatic rifts? LiDAR and InSAR observations of the Dabbahu rift segment, Afar, Ethiopia*, University of Leeds.
- Karner, G. D., and N. W. Driscoll (1999), Style, timing and distribution of tectonic deformation across the exmouth plateau, northwest australia, determined from stratal architecture and quantitative basin modelling, in *Continental Tectonics. Geological Society, London, Special Publications*, vol. 164, edited by C. MacNiocall and P. D. Ryan,

- pp. 271–311, Geological Society of London.
- Koehn, D., A. Steiner, and K. Aanyu (2019), Modelling of extension and dyking-induced collapse faults and fissures in rifts, *Journal of Structural Geology*, 118, 21–31, doi: 10.1016/j.jsg.2018.09.017.
- Longley, I. M., C. Buessenschuett, L. Clydsdale, C. J. Cubitt, R. C. Davis, M. K. Johnson, N. M. Marshall, A. P. Murray, R. Somerville, T. B. Spry, and Others (2002), The north west shelf of australia—a woodside perspective, in *The sedimentary basins of Western Australia 3*, vol. 3, edited by M. Keep and S. J. Moss, pp. 27–88, Petroleum Exploration Society of Australia, Perth.
- Macrae, E. J., C. E. Bond, Z. K. Shipton, and R. J. Lunn (2016), Increasing the quality of seismic interpretation, *Interpretation—a Journal of Subsurface Characterization*, 4(3), T395–T402, doi: 10.1190/INT-2015-0218.1.
- Magee, C., and C. A.-L. Jackson (2020), Seismic reflection data reveal the 3D structure of the newly discovered ex-mouth dyke swarm, offshore NW australia, *Solid earth*, 11(2), 579–606, doi: 10.5194/se-11-579-2020.
- Magee, C., and C. A.-L. Jackson (2021), Can we relate the surface expression of dike-induced normal faults to subsurface dike geometry?, *Geology*, 49(4), 366–371, doi: 10.1130/G48171.1.
- Magee, C., and V. Love (2021), Dyke-induced fault measurements and predicted dyke properties offshore NW australia, doi: 10.5285/f8c2c92a-450d-49e7-bfac-9317d2828e33.
- Magee, C., O. B. Duffy, K. Purnell, R. E. Bell, C. A.-L. Jackson, and M. T. Reeve (2016), Fault-controlled fluid flow inferred from hydrothermal vents imaged in 3D seismic reflection data, offshore NW australia, *Basin Research*, 28(3), 299–318, doi: 10.1111/bre.12111.
- Magee, C., C. Kling, P. Byrne, and C. A.-L. Jackson (2022), Seismic reflection data reveal the 3D subsurface structure of pit craters, *Journal of geophysical research. Planets*, 127(8), e2021JE007155, doi: 10.1029/2021je007155.
- Mansfield, C. S., and J. A. Cartwright (1996), High resolution fault displacement mapping from three-dimensional seismic data: evidence for dip linkage during fault growth, *Journal of Structural Geology*, 18(2-3), 249–263, doi: 10.1016/s0191-8141(96)80048-4.
- Martin, J., A. M. Fernandes, J. Pickering, N. Howes, S. Mann, and K. McNeil (2018), The stratigraphically preserved signature of persistent backwater dynamics in a large paleodelta system: The mungaroo formation, north west shelf, australia, *Journal of Sedimentary Research*, 88(7), 850–872, doi: 10.2110/jsr.2018.38.
- Mastin, L. G., and D. D. Pollard (1988), Surface deformation and shallow dike intrusion processes at inyo craters, long valley, california, *Journal of geophysical research*, 93(B11), 13,221–13,235, doi: 10.1029/jb093ib11p13221.
- Norcliffe, J., C. Magee, C. Jackson, J. Kopping, and B. Lathrop (2021), Fault inversion contributes to ground deformation above inflating igneous sills, *Volcanica*, 4(1), 1–21, doi: 10.30909/vol.04.01.0121.
- Pansino, S., A. Emadzadeh, and B. Taisne (2019), Dike channelization and solidification: Time scale controls on the geometry and placement of magma migration pathways, *Journal of Geophysical Research, [Solid Earth]*, 124(9), 9580–9599, doi: 10.1029/2019jb018191.
- Paumard, V., J. Bourget, T. Payenberg, R. B. Ainsworth, A. D. George, S. Lang, H. W. Posamentier, and D. Peyrot (2018), Controls on shelf-margin architecture and sediment partitioning during a syn-rift to post-rift transition: Insights from the barrow group (northern carnarvon basin, north west shelf, australia), *Earth-Science Reviews*, 177, 643–677, doi: 10.1016/j.earscirev.2017.11.026.
- Perrin, C., A. Jacob, A. Lucas, R. Myhill, E. Hauber, A. Batov, T. Gudkova, S. Rodriguez, P. Lognonné, J. Stevanović, M. Drilleau, and N. Fuji (2022), Geometry and segmentation of cerberus fossae, mars: Implications for marsquake properties, *Journal of geophysical research. Planets*, 127(1), e2021JE007118, doi: 10.1029/2021JE007118.
- Poland, M. P., W. P. Moats, and J. H. Fink (2008), A model for radial dike emplacement in composite cones based on observations from summer coon volcano, colorado, USA, *Bulletin of Volcanology*, 70(7), 861–875, doi: 10.1007/s00445-007-0175-9.
- Pollard, D. D., and P. Segall (1987), Theoretical displacements and stresses near fractures in rock: with applications to faults, joints, veins, dikes, and solution surfaces, in *Fracture mechanics of rock*, edited by B. K. Atkinson, pp. 277–347, Academic Press, London.
- Pollard, D. D., and M. R. Townsend (2018), Fluid-filled fractures in earth's lithosphere: Gravitational loading, interpenetration, and stable height of dikes and veins, *Journal of Structural Geology*, 109, 38–54, doi: 10.1016/j.jsg.2017.11.007.
- Pollard, D. D., P. T. Delaney, W. A. Duffield, E. T. Endo, and A. T. Okamura (1983), Surface deformation in volcanic rift zones, *Tectonophysics*, 94(1-4), 541–584, doi: 10.1016/0040-1951(83)90034-3.
- Pryer, L. L., K. K. Romine, T. S. Loutit, and R. G. Barnes (2002), Carnarvon basin architecture and structure defined by the integration of mineral and petroleum exploration tools and techniques, *The APPEA journal*, 42(1), 287, doi: 10.1071/aj01016.
- Rankey, E. C., and J. C. Mitchell (2003), That's why it's called interpretation: Impact of horizon uncertainty on seismic attribute analysis, *Leading Edge*, 22(9), 820–828, doi: 10.1190/1.1614152.
- Reeve, M. T., C. A.-L. Jackson, R. E. Bell, C. Magee, and I. D. Bastow (2016), The stratigraphic record of pre-breakup geodynamics: Evidence from the barrow delta, offshore northwest australia, *Tectonics*, 35(8), 1935–1968, doi: 10.1002/2016tc004172.
- Reeve, M. T., C. Magee, I. D. Bastow, C. McDermott, C. A.-L. Jackson, R. E. Bell, and J. Prytulak (2021), Nature of the cuvier abyssal plain crust, offshore NW australia, *Journal of the Geological Society*, 178(5), doi: 10.1144/jgs2020-172.
- Rivalta, E., B. Taisne, A. P. Bungler, and R. F. Katz (2015), A review of mechanical models of dike propagation: Schools of thought, results and future directions, *Tectonophysics*, 638, 1–42, doi: 10.1016/j.tecto.2014.10.003.
- Rivas-Dorado, S., J. Ruiz, and I. Romeo (2021), Subsurface geometry and emplacement conditions of a giant dike system in elysium fossae, mars, *Journal of geophysical research. Planets*, 126(1), e2020JE006512, doi: 10.1029/2020je006512.
- Robb, M. S., B. Taylor, and A. M. Goodliffe (2005), Re-examination of the magnetic lineations of the gascoyne and cuvier abyssal plains, off NW australia, *Geophysical Journal International*, 163(1), 42–55, doi: 10.1111/j.1365-246X.2005.02727.x.
- Rowland, J. V., E. Baker, C. J. Ebinger, D. Keir, T. Kidane, J. Biggs, N. Hayward, and T. J. Wright (2007), Fault growth

- at a nascent slow-spreading ridge: 2005 dabbahu rifting episode, afar, *Geophysical Journal International*, 171(3), 1226–1246, doi: 10.1111/j.1365-246x.2007.03584.x.
- Rubin, A. M. (1992), Dike-induced faulting and graben subsidence in volcanic rift zones, *Journal of geophysical research*, 97(B2), 1839–1858, doi: 10.1029/91jb02170.
- Rubin, A. M. (1993), Tensile fracture of rock at high confining pressure: Implications for dike propagation, *Journal of geophysical research*, 98(B9), 15,919, doi: 10.1029/93jb01391.
- Rubin, A. M., and D. D. Pollard (1988), Dike-induced faulting in rift zones of iceland and afar, *Geology*, 16(5), 413, doi: 10.1130/0091-7613(1988)016<0413:difirz>2.3.co;2.
- Schaaf, A., and C. E. Bond (2019), Quantification of uncertainty in 3-D seismic interpretation: implications for deterministic and stochastic geomodeling and machine learning, *Solid earth*, 10(4), 1049–1061, doi: 10.5194/se-10-1049-2019.
- Schöpfer, M. P. J., C. Childs, and J. J. Walsh (2006), Localisation of normal faults in multilayer sequences, *Journal of Structural Geology*, 28(5), 816–833, doi: 10.1016/j.jsg.2006.02.003.
- Shibley, T. F., and B. Tikoff (2016), Linking cognitive science and disciplinary geoscience practice: The importance of the conceptual model, in *3-D Structural Interpretation: Earth, Mind and Medicine*, vol. Memoir 111, AAPG Special Volumes.
- Shipton, Z. K., J. J. Roberts, E. L. Comrie, Y. Kremer, R. J. Lunn, and J. S. Caine (2020), Fault fictions: Systematic biases in the conceptualization of fault-zone architecture, *Geological Society special publication*, 496(1), 125–143.
- Stagg, H. M. J., M. B. Alcock, G. Bernardel, A. M. G. Moore, P. A. Symonds, and N. F. Exon (2004), *Geological Framework of the Outer Exmouth Plateau and Adjacent Ocean Basins*, Geoscience Australia.
- Taylor, S. K., A. Nicol, and J. J. Walsh (2008), Displacement loss on growth faults due to sediment compaction, *Journal of Structural Geology*, 30(3), 394–405, doi: 10.1016/j.jsg.2007.11.006.
- Tentler, T. (2005), Propagation of brittle failure triggered by magma in iceland, *Tectonophysics*, 406(1), 17–38, doi: 10.1016/j.tecto.2005.05.016.
- Tibaldi, A., F. L. Bonali, N. Corti, E. Russo, K. Drymoni, E. De Beni, S. Branca, M. Neri, M. Cantarero, and F. P. Mariotto (2022), Surface deformation during the 1928 fissure eruption of mt. etna (italy): Insights from field data and FEM numerical modelling, *Tectonophysics*, 837(229468), 229,468, doi: 10.1016/j.tecto.2022.229468.
- Tindale, K., N. Newell, J. Keall, and N. Smith (1988), Structural evolution and charge history of the exmouth sub-basin, northern carnavon basin, western australia, in *The Sedimentary Basins of Western Australia 2: Proc. of Petroleum Society Australia Symposium*, Perth, WA, pp. 473–490.
- Townsend, M. R., D. D. Pollard, and R. P. Smith (2017), Mechanical models for dikes: A third school of thought, *Tectonophysics*, 703-704, 98–118, doi: 10.1016/j.tecto.2017.03.008.
- Trippanera, D., V. Acocella, J. Ruch, and B. Abebe (2015a), Fault and graben growth along active magmatic divergent plate boundaries in iceland and ethiopia, *Tectonics*, 34(11), 2318–2348, doi: 10.1002/2015tc003991.
- Trippanera, D., J. Ruch, V. Acocella, and E. Rivalta (2015b), Experiments of dike-induced deformation: Insights on the long-term evolution of divergent plate boundaries, *Journal of Geophysical Research, [Solid Earth]*, 120(10), 6913–6942, doi: 10.1002/2014jb011850.
- Trippanera, D., J. Ruch, L. Passone, and S. Jónsson (2019), Structural mapping of dike-induced faulting in harrat lunayyir (saudi arabia) by using high resolution drone imagery, *Frontiers of earth science*, 7, 168, doi: 10.3389/feart.2019.00168.
- Urbani, S., V. Acocella, E. Rivalta, and F. Corbi (2017), Propagation and arrest of dikes under topography: Models applied to the 2014 bardarbunga (iceland) rifting event, *Geophysical research letters*, 44(13), 6692–6701, doi: 10.1002/2017gl073130.
- von Hagke, C., M. Kettermann, N. Bitsch, D. Bücken, C. Weismüller, and J. L. Urai (2019), The effect of obliquity of slip in normal faults on distribution of open fractures, *Frontiers of earth science*, 7(18), doi: 10.3389/feart.2019.00018.
- Wilson, C. G., C. E. Bond, and T. F. Shipley (2019), How can geologic decision-making under uncertainty be improved?, *Solid earth*, 10(5), 1469–1488, doi: 10.5194/se-10-1469-2019.
- Wilson, L., and J. W. Head (2002), Tharsis-radial graben systems as the surface manifestation of plume-related dike intrusion complexes: Models and implications, *Journal of geophysical research*, 107(E8).
- Woods, J., T. Winder, R. S. White, and B. Brandsdóttir (2019), Evolution of a lateral dike intrusion revealed by relatively-relocated dike-induced earthquakes: The 2014–15 Bárðarbunga–Holuhraun rifting event, iceland, *Earth and planetary science letters*, 506, 53–63, doi: 10.1016/j.epsl.2018.10.032.
- Wright, T. J., C. Ebinger, J. Biggs, A. Ayele, G. Yirgu, D. Keir, and A. Stork (2006), Magma-maintained rift segmentation at continental rapture in the 2005 afar dyking episode, *Nature*, 442(7100), 291–294, doi: 10.1038/nature04978.
- Xu, W., S. Jónsson, F. Corbi, and E. Rivalta (2016), Graben formation and dike arrest during the 2009 harrat lunayyir dike intrusion in saudi arabia: Insights from InSAR, stress calculations and analog experiments, *Journal of Geophysical Research, [Solid Earth]*, 121(4), 2837–2851, doi: 10.1002/2015jb012505.
- Yang, X.-M., and C. Elders (2016), The mesozoic structural evolution of the gorgon platform, north carnavon basin, australia, *Australian Journal of Earth Sciences*, 63(6), 755–770, doi: 10.1080/08120099.2016.1243579.